Catalysis Science & Technology

ROYAL SOCIETY OF CHEMISTRY

PAPER

View Article Online
View Journal | View Issue

Cite this: *Catal. Sci. Technol.*, 2023, 13, 5387

CeO_2-supported Ni and Co catalysts prepared by a solution combustion method for H_2 production from glycerol: the effect of fuel/oxidizer ratio and oxygen excess†

Anna N. Matveyeva, *[a] Shamil O. Omarov, [a] Marianna A. Gavrilova,[ab] Andrey D. Trofimuk,[c] Johan Wärnå[d] and Dmitry Yu. Murzin *[d]

Received 21st June 2023,
Accepted 3rd August 2023

DOI: 10.1039/d3cy00854a

rsc.li/catalysis

Glycerol is a promising raw material for obtaining various chemicals and fuels, including H_2. Nevertheless, the development of cost-effective and stable catalysts with high activity and selectivity for H_2 production from glycerol under mild conditions has been a serious problem for their practical use. In this work, a series of CeO_2-supported Ni and Co catalysts with the content of Ni and Co as metal(II) oxides being 30 wt% was prepared by solution combustion synthesis *via* changing the fuel/oxidizer ratio (φ = 0.7–3), the fuel type (glycine, urea), and the oxygen excess. Thus, various species of Ni and Co and their interactions with CeO_2 were obtained, which affected the reduction sequence, defectiveness, textural characteristics, and activity in steam and aqueous-phase reforming of glycerol. To study the characteristics of the obtained samples, instrumental methods such as XRD, DTA-TGA, low-temperature N_2 physisorption, SEM-EDX, H_2-TPR, and H_2- and CO_2-TPD, as well as Raman spectroscopy, were used. The results demonstrated that the Ni–Ce–O system synthesized with a high glycine-to-oxidizer ratio can successfully compete with catalysts based on noble metals (Pt/γ-Al_2O_3) in aqueous-phase reforming of glycerol.

1. Introduction

One of the consequences of global population growth and industrialization is the depletion of fossil fuels, the use of which has also exacerbated global warming and climate change.[1] Among the alternatives to fossil sources, hydrogen (H_2) has emerged as an energy vector of the future.[2] Hydrogen is predicted to be the main source of 90% of the world's energy by 2080.[3] One of the effective and promising methods of hydrogen production is steam (SR) and aqueous-phase reforming (APR) of glycerol.[4] The latter is a by-product of the growing biodiesel industry, as a result of which the glycerol production has increased significantly in the few recent years, saturating the market and causing a free fall in prices.[5,6] In this context, it is important to manage excess glycerol to avoid waste problems and adverse effects on biodiesel industrial development.[7]

APR of glycerol compared to steam reforming is more preferable for hydrogen production in terms of side reactions, as well as more thermodynamically favorable conditions (200–260 °C; 20–50 bar) for the water–gas shift (WGS) reaction.[3,8] The latter is especially important in the case of subsequent use of hydrogen in fuel cells that are sensitive to CO.[9] In addition, APR of glycerol is an alternative to SR when glycerol is already obtained dissolved in H_2O, in particular, in upstream biomass processing.

Steam reforming, which proceeds at higher temperatures and lower pressures, in contrast, imposes more stringent requirements regarding the thermal stability of the catalyst, especially in the presence of steam, as well as resistance to carburization. The latter issue is one of the main causes of catalyst deactivation, together with metal particle sintering.

In the few recent years, various combinations of catalysts and supports have been reported in the literature about reforming processes of glycerol. Among them, catalysts based on transition metals, in particular Ni and Co, are more preferable due to low costs and wide availability.

Ni-containing catalysts are known to have a high capability for C–C, C–H and O–H bond cleavage[10] and can be

[a] *Laboratory of Materials and Processes for Hydrogen Energy, Ioffe Institute, Politekhnicheskaya ul. 28, 194021 St. Petersburg, Russia. E-mail: anna.matveyeva@mail.ioffe.ru*
[b] *Department of Physical Chemistry, St. Petersburg State Institute of Technology (Technical University), Moskovskiy pr. 26, 190013 St. Petersburg, Russia*
[c] *Laboratory of Physics for Cluster Structures and Colloid Physics Laboratory, Ioffe Institute, Politekhnicheskaya ul. 28, 194021 St. Petersburg, Russia*
[d] *Laboratory of Industrial Chemistry and Reaction Engineering, Åbo Akademi University, Henriksgatan 2, 20500 Turku/Åbo, Finland. E-mail: dmurzin@abo.fi*
† Electronic supplementary information (ESI) available. See DOI: https://doi.org/10.1039/d3cy00854a

easily dispersed on a range of supports. A number of nickel catalysts supported on Al_2O_3,[11–20] CeO_2,[17,20–37] MgO,[21,22,30] TiO_2,[21,22,38] SiO_2,[13,38–40] and ZrO_2 (ref. 13, 38, and 41–44) have been studied in reforming processes of several renewable feeds, including methanol,[9] ethanol,[14–17,24,26,27,32–34,37,39,41] and glycerol.[11–13,20–23,25,28–31,35,36,38,40,42–44] Al_2O_3 and CeO_2 as supports are considered effective in terms of high H_2 production and lower coke formation.[17] However, according to ref. 23, Ni supported on CeO_2 has a higher stability in glycerol steam reforming compared to Ni/Al_2O_3, despite having a significantly lower specific surface area. A comparative study of nickel catalyst deactivation on Al_2O_3, CeO_2, ZnO, MgO, ZrO_2, and SiO_2 in low-temperature steam reforming of ethanol showed the following decreasing order of activity: $CeO_2 > Al_2O_3 > ZrO_2$.[45]

The excellent stability of Ni/CeO_2 has been related to accelerated carbon removal from the metal surface due to the mobility of oxygen ions and formation of oxygen vacancies in the support.[46] Recent studies of Ni/CeO_2 systems in reforming processes are related to controlling the functional properties of catalysts through changing the morphology,[32,33,36] preparation methods,[24,28,34,35] active component content,[24] promoters,[26,47] and additives.[27,48,49]

Although Co-based catalysts supported on CeO_2 have not been studied for glycerol reforming as extensively as nickel-based catalysts,[50] they have also been reported to demonstrate excellent ethanol steam reforming activity.[34,37,51–58] It has been found that Co/CeO_2 exhibited optimum hydrogen yield and stability compared to Fe-, Ni-, and Cu-based catalysts.[37] Recent studies of Co/CeO_2 systems in reforming processes are associated with the modification of the support and/or active phase,[56] and changing the cobalt content[58] and its dispersion,[34] or the CeO_2 crystal facet[59] to fine-tune the local structure of the surface.

It is well known that material preparation methods have a strong effect on the structural, textural, and catalytic properties. For Ni and Co-based catalyst preparation, the incipient wetness impregnation[22,24,28,32,35–37,52,53,57] and wet impregnation[21,25,29,49] methods are mainly used. However, these methods have limitations in the synthesis of a catalyst with a high content of the active component, at which it is difficult to achieve high metal dispersion. A small particle size with a uniform distribution of active components can also be achieved by the co-precipitation method even at a high metal content.[15,58] The disadvantages of this method include a long duration and the overall complexity, careful control of the synthesis conditions, and precipitation and washing completeness. In addition, the precipitation methods are characterized by a significant consumption of reagents and large amounts of wastewater.

Therefore, other alternative methods for the formation of inorganic materials, such as the solution combustion synthesis (SCS) method, are becoming more widespread. SCS involves the rapid heating of a solution containing certain amounts of an oxidizing agent (metal precursors, often nitrates) and an organic fuel such as urea, glycine or citric acid. The combustion technique allows obtaining very fine crystalline oxide powders of high purity with a homogeneous, non-agglomerated and multicomponent composition.[60] Some studies show that catalysts prepared using this method are comparable with catalysts obtained by classical methods, for example Ni-based supported catalysts for ethanol decomposition and reforming.[26,27,31,61–63] In addition, a high conversion of glycerol (30%) was obtained for the 20 wt% Ni-based catalyst on CeO_2 synthesized by the self-propagation combustion method compared to those by co-precipitation or wet impregnation due to the formation of smaller nickel crystallites.[29]

Fuel usually plays a central role in optimizing material properties because it often performs the triple function of a reducing and a complexation agent, and a microstructural template.[64,65] However, the characteristics of the final powder obtained by the SCS method also depend on other synthesis parameters, such as the fuel-to-oxidizer ratio (φ), metal precursor type, chemical composition, pH, heating method, *etc.* Subsequently, the main drawback of this method is the difficulties in defining the optimal fuel-to-oxidizer ratio. The amount of fuel calculated directly from the stoichiometric ratio for combustion results frequently in a product of an undesired composition.[66]

There are several studies on Ni–Ce and Co–Ce oxide systems prepared by the SCS method, focused on the effect of Sn and Zr,[26] NaCl,[67] and colloidal SiO_2 (ref. 68 and 69) (using glycine fuel), Ni loading (0–8.5 wt%, urea;[31] 3–68 wt%, hydrous hydrazine;[70] 3.1–15.6 wt%, urea[71]), Co loading (1–10 wt%, glycine[69]), the fuel-to-oxidizer ratio (φ = 0.5–3, hydrous hydrazine[70]), and the fuel type (glycine and hydrous hydrazine at φ = 2;[70] oxalyldihydrazide, glycerol, carbohydrazide, urea at φ = 1 (ref. 71)) on their physical, chemical, and catalytic properties in various processes. However, no attention was paid to the features of their formation upon varying the ratio of glycine and urea to the oxidizing agent and their influence on the catalytic behavior during glycerol reforming. The ratio of fuel/oxidizer is one of the most important parameters affecting not only the phase composition, but also the structure, defectiveness, and related properties of the materials. Therefore, the present study aims to comparatively explore CeO_2-supported Ni and Co catalysts prepared by varying the SCS parameters, such as the fuel type (glycine, urea), the fuel-to-oxidizer ratio, and the oxygen excess, in both steam and aqueous-phase reforming of glycerol.

2. Experimental

2.1. Reagents

$Ni(NO_3)_2{\cdot}6H_2O$ (99.2%, Lenreactiv, Russia), $Co(NO_3)_2{\cdot}6H_2O$ (97%, Lenreactiv, Russia), $Ce(NO_3)_3{\cdot}6H_2O$ (99.8%, Chemcraft, Russia), ammonium nitrate (98.5%, Russia), glycine (99.2%, Lenreactiv, Russia), urea (99.8%, Lenreactiv, Russia), AlOOH (Catapal, Sasol), H_2PtCl_6 (37 wt% Pt), and glycerol (99.3%, Lenreactiv, Russia) were used.

2.2. Preparation

An appropriate amount of glycine (or urea) and the corresponding metal nitrates were dissolved in DI water (1 mL per 1 g of the starting materials) in a wide glass beaker (250 mL) to obtain 1 g of NiO/CeO_2 or CoO/CeO_2. The theoretical content of nickel and cobalt calculated as NiO and CoO was 30 wt%. In some syntheses, 1 g of NH_4NO_3 was additionally used per 1 g of NiO/CeO_2. The fuel-to-oxidizer ratio (φ) was taken from 0.7 to 3 and calculated *via* the reducing and oxidizing valence states (RV and OV, respectively) according to ref. 65 and 72:

$$\varphi = (-1)\sum(\text{coeff.}\cdot\text{RV of fuel})/\sum(\text{coeff.}\cdot\text{OV of nitrate}), \quad (1)$$

The methodology for calculating the reducing and oxidizing valence states can be found in ref. 73. By selecting the ratio between reagents, the value of φ can be changed. For example, the reaction equation occurring with glycine at $\varphi = 1$ $(-1\cdot9\cdot100/(-15\cdot36 + (-10)\cdot36)$ can be represented as:

$$36Ce(NO_3)_3(aq) + 36Ni(NO_3)_2(aq) + 100C_2H_5NO_2 + 9O_2 \rightarrow 36(NiO\cdot CeO_2) + 200CO_2 + 140N_2 + (250H_2O), \quad (2)$$

The resulting aqueous solution of fuel with salts was heated on an electric plate (1 kW) to boiling. It was burned with the formation of a solid powder, after complete evaporation of H_2O. To avoid oxidation of the resulting combustion products, the beaker was covered with a Petri dish immediately after the end of combustion (denoted with *). Two or three batches of each catalyst were synthesized. Reaction equations for each synthesis can be found in the ESI.†

A platinum–alumina (Pt/Al_2O_3) catalyst was synthesized by impregnation of γ-Al_2O_3 (prepared by calcining AlOOH at 700 °C) with an excess of H_2PtCl_6 solution to obtain 1 wt% Pt. After impregnation, the sample was dried and heat-treated at 260 °C (according to ref. 74) in an oven. The catalyst was reduced in a reactor at 280 °C prior to experiments as discussed below.

2.3. Characterization

XRD analysis was done on a Rigaku SmartLab 3 diffractometer (Japan) equipped with a 1D DteX250 detector (Rigaku, Japan) and Ni-filter (Rigaku, Japan) at λ = 1.54056 Å, 30 mA, 40 kV, a 4° min^{-1} scan speed, and a 0.01° step width. The diffraction data were analyzed by the Rietveld method. The refinement procedure and software are similar to those given in ref. 69. The structural parameters for CeO_2 (no. 193169), NiO (no. 184918), Ni (no. 426960), CoO (no. 245319), Co_3O_4 (no. 290720) and Co (no. 622442) with the space group $Fm\bar{3}m$ were taken using the ICDD PDF-2 database.

N_2-physisorption data were obtained on Quantachrome's Autosorb-6iSA (USA) and Micromeritics ASAP 2020 (USA) units. The samples were preliminarily degassed at 200–250 °C under vacuum. The specific surface area, the total pore volume, and the average pore diameter were determined using the BET equation, while the distribution of pore size was obtained by the NLDFT method.

SEM was carried out on a TESCAN VEGA 3 SBH microscope (Czech Republic) equipped with an INCAx-act EDS detector (Oxford Instruments).

H_2-TPR, H_2-TPD, and CO_2-TPD were performed on a SOLO Chemosorb (Russia) equipped with a TCD (thermal conductivity detector). In H_2-TPR tests, *ca.* 30 mg of powder without pretreatment was reduced from 80–100 to 620–720 °C at a 10 °C min^{-1} rate under 20 mL min^{-1} of 10 vol% H_2/Ar (99.998 vol% purity). 2-Propanol cooled in liquid N_2 was used to trap water vapor.

For H_2-TPD, *ca.* 100 mg of a sample was first reduced *in situ* with a H_2/Ar flow (50 : 50 vol%, 40 mL min^{-1}) at a ramp rate of 20 °C min^{-1} to 450 °C and 10 °C min^{-1} to 500 °C and held for 30 min. Then, it was cooled to 60 °C and saturated with H_2 (H_2/Ar flow, 50 : 50 vol%, 20 mL min^{-1}) for 20 min. After removing the physically adsorbed H_2 by purging with Ar (20 mL min^{-1}), the sample was heated to 700–800 °C at a ramping rate of 10 °C min^{-1}. The nickel dispersion (D_{Ni}, %), specific metal surface area (A, m^2 g^{-1} Ni), and the average Ni diameter (d, nm) were calculated by assuming a stoichiometric ratio of H/Ni using the following equations:[75]

$$D = \frac{N_S}{N_T} = \frac{2\cdot V_{H_2}/V_m}{m_{cat}\cdot\omega_{Ni}/M_{Ni}}\cdot N_A, \quad (3)$$

$$A = \frac{a_m\cdot N_s}{m_{cat}\cdot\omega_{Ni}}, \quad (4)$$

$$d = \frac{6\cdot v_m}{a_m\cdot D}, \quad (5)$$

where N_S is the number of surface atoms; N_T – the total number of atoms; V_{H_2} – the volume of desorbed H_2, μL; V_m – the molar volume, μL; N_A – the Avogadro number; m_{cat} – the catalyst mass, g; ω_{Ni} – the Ni loading, wt%; M_{Ni} – the molar mass of Ni, g mol^{-1}; a_m (6.51×10^{-20} for Ni) – the area occupied by a surface atom, m^2; v_m (10.95×10^{-30} for Ni) – the volume occupied by an atom in the bulk metal, m^3.

For CO_2-TPD, 100–200 mg of a sample was first reduced *in situ* with a H_2/He flow (50 : 50 vol%, 40 mL min^{-1}) at a ramp rate of 20 °C min^{-1} to 450 °C and 10 °C min^{-1} to 520 °C and held for 30 min. Then, it was cooled to 110 °C and saturated with CO_2 (CO_2/He flow, 10 : 90 vol%, 20 mL min^{-1}) for 20 min. After removing the physically adsorbed CO_2 by purging with He (20 mL min^{-1}), the sample was heated to 600 °C at a ramping rate of 10 °C min^{-1}.

Raman patterns were obtained using an NTEGRA Spectra spectrometer ("NT-MDT", Russia) equipped with a 532.01 nm diode laser, a 100× objective and a 1800 lines per mm grating. The measurements were carried out at room temperature. To prevent sample heating, a beam with a power density <50 W cm^{-2} was used. Spectra were recorded at several random points, with each graph representing the average spectrum for a sample.

A simultaneous thermal analysis was done on a Shimadzu DTG-60A analyzer (Japan) by heating a sample in static air to 800 °C with a ramp rate of 10 °C min^{-1}.

2.4. Catalytic tests

2.4.1. Glycerol steam reforming (GSR). Glycerol steam reforming was carried out at atmospheric pressure and 520 °C in a stainless-steel reactor (50 cm in length, 10 mm in diameter) with a fixed catalyst bed (7–40 mg). The catalyst was first exposed to a N_2 flow (99.999 vol% purity, 30 mL min^{-1}), heated to 520 °C and reduced at this temperature with 40 mL min^{-1} of 50 vol% H_2/N_2 for 30 min. After catalyst reduction, the reactor was purged with a N_2 flow for 5–10 min. For all tests, the reactor was fed with a flow of N_2 (30 mL min^{-1}) and liquid feedstock (a mixture of 20 wt% glycerol with double distilled water; water-to-glycerol feed ratio = 20 : 1; total liquid flow 7.2–16.6 mL h^{-1}). The resulting gaseous products were accumulated in a gas holder for sampling for 5–7 min with fixation of the volume of the formed gas. The duration of the tests did not exceed 2 h. The gaseous products were analyzed on a Shimadzu GC-2010 Plus chromatograph (Japan) with a TCD and RT-Msieve 5A and Rt-Q-BOND capillary columns. The heating program was similar to a program used in previous studies.[31,42]

The glycerol conversion to gaseous products (X_{Ggas}, %), hydrogen yield ($Y(H_2)$, %), and selectivity to H_2, CO_2, CO, CH_4, C_2H_4, C_2H_6, and C_3H_8 (S(i), mol%) were calculated according to the following equations:

$$X_{Ggas} = \frac{\text{Total molar C of gas products}}{\text{Molar flow C of glycerol in the feedstock}} \cdot 100\%, \quad (6)$$

$$Y(H_2) = \frac{\text{Molar flow of } H_2}{7 \cdot \text{Molar flow of glycerol in the feedstock}} \cdot 100\%, \quad (7)$$

$$S(H_2) = \frac{\text{Molar flow of } H_2}{\text{Total molar C of gas products}} \cdot \frac{3}{7} 100\%, \quad (8)$$

$$S(i) = \frac{\text{Molar flow C of i}}{\text{Total molar C of gas products}} \cdot 100\%, \quad (9)$$

where i – carbon-based gaseous product (*e.g.* CO, CH_4, *etc.*); molar flow C of i – molar flow of the product multiplied by the number of "C" atoms in the compound, mol h^{-1}; 3 and 7 – stoichiometric coefficients from the equation: $C_3H_8O_3 + 3H_2O = 3CO_2 + 7H_2$.

The deactivation constant (k_d) was determined by fitting the dependence of hydrogen yield on TOS in accordance with the equation:

$$a = a_t e^{-k_d t} + a_\infty = (a_0 - a_\infty) e^{-k_d t} + a_\infty, \quad (10)$$

where a is the yield of hydrogen, a_∞ is the hydrogen yield at complete deactivation, and a_t is the pre-exponential parameter for the time (t) dependence of the hydrogen yield, equal in the current study to $a_0 - a_\infty$, where a_0 is the initial yield of hydrogen at TOS = 0.

The hydrogen formation rate (mol H_2 per mol Ni per s) was also calculated:

$$r(H_2) = \left(\frac{Y(H_2) \cdot V_{lq} \cdot \rho_{lq} \cdot w_G}{M_G}\right) \cdot \left(\frac{M_{Ni}}{m_{cat} \cdot w_{Ni} \cdot 3600}\right), \quad (11)$$

where $Y(H_2)$ – the hydrogen yield, mol H_2 per mol glycerol; V_{lq} – the total liquid flow of the feedstock (glycerol and water), mL h^{-1}; ρ_{lq} – the density of a glycerol–water mixture at 20 °C, g mL^{-1}; w_G and w_{Ni} – the mass fractions of glycerol in the feedstock and nickel in the catalyst; M_G and M_{Ni} – molar masses of glycerol and nickel, g mol^{-1}; 3600 – time conversion factor.

The weight hourly space velocity (WHSV, h^{-1}) was calculated as:

$$WHSV = V_{lq} \cdot \rho_{lq} / m_{cat}, \quad (12)$$

2.4.2. Glycerol aqueous-phase reforming (GAPR). A once-through plug-flow reactor (8 mm diameter, 20 cm length) was used with a catalyst load of 200–668 mg between quartz layers (load 4 cm^3). The set-up for aqueous-phase reforming of glycerol is similar to that used in ref. 76. Before testing, the samples were preliminarily reduced at 280–332 °C in accordance with the results of H_2-TPR for 1–2 h in a H_2 flow (30 mL min^{-1}) at 34 bar. The catalytic experiments were performed at the same pressure and 231 °C. During all tests, the reactor was exposed to a N_2 flow (99.999 vol% purity, 40 mL min^{-1}) and liquid feedstock (glycerol : water = 10 : 90 wt%, total liquid flow rate 3–9.8 mL h^{-1}). Detailed test conditions are given in the corresponding figure captions. The gas sampling and analysis procedure is similar to the test procedure for glycerol steam reforming.

3. Results and discussion

3.1. Ce–Ni–O: synthesis features and phase composition

Fig. 1 presents the visual course of the combustion process of glycine–nitrate solutions and the macromorphology of the obtained Ce–Ni-containing materials. Under fuel deficit conditions (φ = 0.72), the thermal decomposition of nitrates dominates, as evidenced by the release of a brown gas. The most pronounced ignition is observed at the stoichiometric fuel-to-oxidizer ratio (φ = 1), which, however, entails the greatest entrainment of powder particles from the reaction zone. The powders remaining in the beaker and outside were analyzed separately using simultaneous thermal analysis (Fig. 2). Due to the fact that the combustion mode is disturbed, the escaped particles are characterized by large weight losses during heating in air compared to the sample remaining in the beaker (Fig. 2a).

It should be noted that with greater contact of the solid products with oxygen (in the case of particle entrainment, φ = 1.25–1.4), the color of the samples changes from black to brown, which can indicate the formation of metallic nickel during combustion and its further oxidation. This assumption is supported by the results shown earlier in ref.

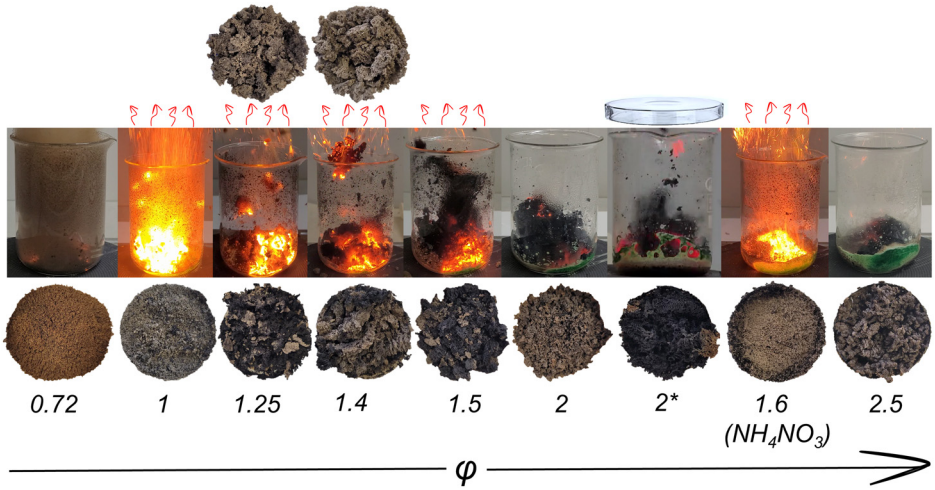

Fig. 1 The course of the glycine–nitrate solution combustion and macromorphology of the Ce–Ni–O systems obtained at various fuel-to-oxidizer ratios. φ = 2* – the beaker was covered with a Petri dish immediately after completion of combustion; φ = 1.6 – ammonium nitrate was additionally used, while maintaining the glycine-to-nitrate ratio equal to 2.

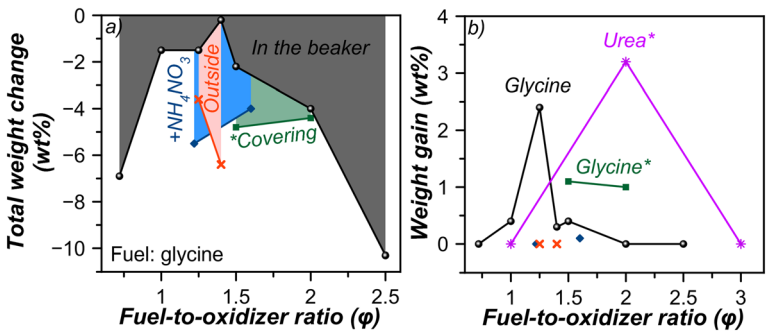

Fig. 2 Total weight change (a) and weight gain (b) during heating in air for the as-prepared Ce–Ni–O systems produced using different conditions.

77–80, where metallic Ni is easily formed from nickel nitrate under fuel rich conditions without any post-reduction treatment. According to ref. 78 and 80, the formation of metallic Ni is triggered by the reducing action of nitrogen oxides and NH_3 or CO produced by the fuel (urea, glycine, citric acid, hexamethylenetetramine) decomposition. However, there are no data for the formation of nickel during combustion of a mixture of nickel and cerium nitrates with any fuel, which can be explained by calcination of the freshly prepared samples.[29,31,67,68,70,71] In ref. 62, the NiO phase was established as the only combustion product of nickel nitrate with fuel on a porous support in air, regardless of the φ value, which varied between one and three.

An increase in the sample weight during heating in air also indicates the interactions of metal Ni particles with oxygen (Fig. 2b). To minimize these interactions, experiments were carried out by covering the beaker with a Petri dish immediately after the end of combustion, as well as with the addition of NH_4NO_3. The results show that abundant gas evolution when using NH_4NO_3 does not prevent the oxidation of the samples. The most effective approach from this point of view is to cover the beaker, judging by the rich black color (Fig. 1, φ = 2*) and the increase in weight gain when heated in air (Fig. 2b). Minimizing oxygen access in the literature was carried out in various ways, for example, by using a beaker with a perforated rubber plug[81] or conducting an experiment in a completely inert environment.[62] According to the time-resolved XRD experiments performed in ref. 62, allowing the monitoring of the evolution of phase formation during combustion of $Ni(NO_3)_2$ + glycine + NH_4NO_3 + SiO_2 mixture (φ = 3) in air, it turned out that during the first reaction stage, only the Ni phase is detected in the combustion front. In this case, oxygen does not influence the reaction in the combustion front, but it oxidizes nickel later in the post-combustion zone. Therefore, minimizing the time of contact with oxygen after the completion of combustion led to the results described above. It should be noted that the combustion mechanism in the absence of SiO_2 is different.[78]

The carbamide–nitrate solution burns without entrainment of sample particles (Fig. 3). In addition, the macromorphology of the solid products corresponds to that of sintered powder particles, in agreement with literature data. For pure NiO, it has also been previously shown that due to poorer interactions of urea with the metal cations, more spherical particles, harder agglomerates, and a higher

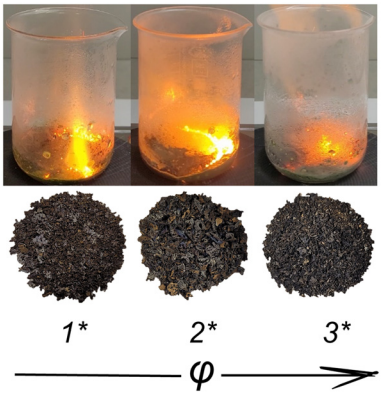

Fig. 3 The carbamide–nitrate solution combustion synthesis and macromorphology of the Ce–Ni–O systems obtained at various fuel-to-oxidizer ratios.

residual carbon content and ability to sinter were obtained compared to those with glycine.[79]

At a urea-to-oxidizer ratio equal to 2, the weight gain is 3.2 wt%, which is the largest among all synthesized Ce–Ni–O systems (Fig. 2b). The total weight change in this case is 0.6 wt%, whereas that at φ = 1 and 3 is *ca.* −6 wt%. It is also important to note that the total weight loss in all cases does not exceed 10.3 wt%, which indicates the efficient course of the combustion process, without the need for further calcination of the samples.

XRD patterns of the obtained Ce–Ni–O systems are presented in Fig. 4. The main reflections correspond to oxide phases of cerium and nickel. After stoichiometric combustion with glycine, in addition to the oxide phases, the presence of metallic nickel is also observed. The metallic phase is also preserved at other fuel-to-oxidizer ratios by limiting the access of oxygen after the completion of combustion.[62] It should be noted that at 2θ = 25.7° (Fig. 4c), a low-intensity reflection peak appears, corresponding to the orthorhombic phase of $CeNiO_3$ (111), the presence of which in trace amounts was typical for most samples. Heat treatment at 700 °C for 6 h did not lead to a change in the intensity of this peak; thus, it cannot be related to the residual fuel or products of its decomposition. Previously, $CeNiO_3$ was reported to be active in dry methane reforming (DRM) to produce syngas.[82] However, during operation, deactivation of the catalyst caused by coke deposits was observed.

In the literature, $CeNiO_3$ was synthesized *via* the co-precipitation method,[83] electrospinning with calcination,[84] the soft-templated sol–gel method with post-calcination,[85] pulsed laser deposition,[86] and the self-combustion method.[82,87] However, in most cases, a mixture of oxides of Ce and Ni is taken as Ce nickelite due to the similarity of most of their reflections.

From the point of view of thermodynamic stability, $CeNiO_3$ has a positive convex hull energy (E_{hull}), signifying its instability, with an absolute value of *ca.* 89 meV per atom, which indicates the release of energy upon decomposition to the stable states CeO_2 and NiO.[88] Nevertheless, a structure exhibiting $E > 0$ does not necessarily mean that the structure cannot exist in nature. There are several examples of metastable structures at 0 K that either become stable at higher temperatures or exist as a kinetically-trapped state. Thus, as far as is known, pure cerium nickelite has not yet been obtained. Samples containing $CeNiO_3$ were synthesized by pulsed laser deposition[86] and the SCS method.[82,87]

The quantitative phase composition, the average crystallite size (D), and unit cell parameters for the Ce–Ni oxide systems were determined by the Rietveld refinement method; the results are presented in Tables 1 and S1† (all data). The phase composition was corrected taking into account the weight gain during heating of the sample in air, which corresponds to the oxidation of metallic nickel and amorphous NiO depending on the stoichiometry and content of crystalline nickel oxide.

As expected, covering makes it possible to preserve a larger fraction of metal in the samples (N. 5-1 and 5-2,

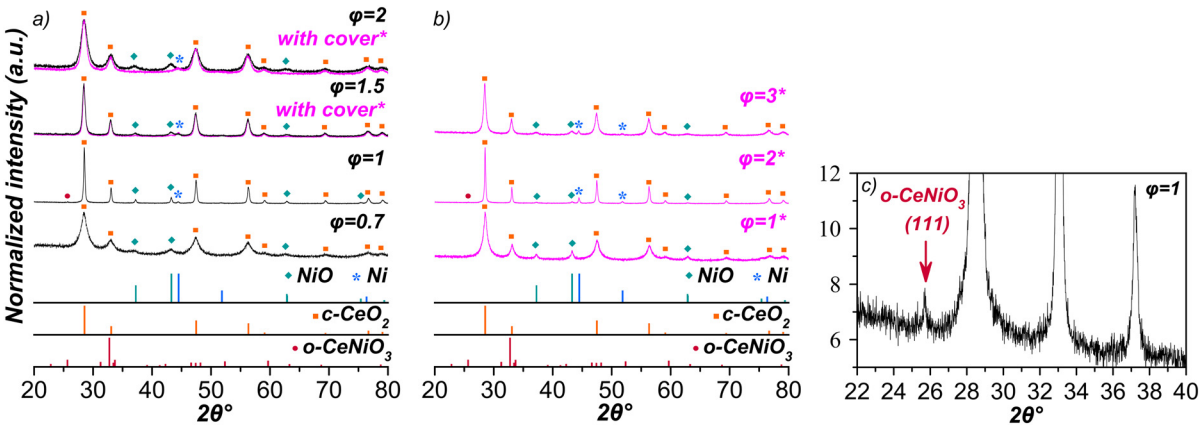

Fig. 4 XRD patterns of Ce–Ni oxide systems obtained by combustion of glycine–nitrate (a and c) and carbamide–nitrate (b) solutions at different fuel-to-oxidizer ratios (φ) (where o-$CeNiO_3$ is orthorhombic $CeNiO_3$ perovskite (Materials Project mp-777024), c-CeO_2 – cubic ceria (JCPDS card no. 01-075-8371), NiO – JCPDS card no. 00-044-1159, Ni – JCPDS no. 00-004-0850, * samples were obtained with covering after the completion of the combustion).

Table 1 Data for the synthesis conditions and phase composition for the Ce–Ni–O systems

N	Fuel	Covering	n(AN)/n(MeN)	φ	Phase composition according to Rietveld/corrected,[b] wt%		
					CeO_2	NiO	Ni
1	Glycine	–	—	0.72	79/67	21/33	0
2[a]		–	—	1	71/67	24/32	5/1
3-1[a]		–	—	1.25	70/67	30/33	0
5-1[a]		–	—	1.5	72/67	21/31	7/2
5-2[a]		+	—	1.5	75/67	9/29	16/4
6-1		–	—	2	73/67	27/33	0
6-2		+	—	2	79/67	0/29	21/4
8[a]		–	1.54	1.6	70/67	23/32	7/1
10	Urea	+	—	1	77/67	23/33	0/0
11[a]		+	—	2	71/67	11/21	18/12
12[a]		+	—	3	71/67	19/no data	10/no data

Note: [a] The sample contains traces of the $CeNiO_3$ phase. [b] Taking into account amorphous nickel oxide and TGA results; n(AN) is the number of moles of ammonium nitrate; n(MeN) is the number of moles of cerium and nickel nitrates.

Table 1). In addition, in this case, the content of amorphous nickel oxide increases from 6–10 to 20–32 wt%, the reason being that the heat released during interactions of nickel with oxygen promotes the crystallization of amorphous nickel oxide. The reproducibility of the phase composition of the samples with the use of covering is shown in Fig. S1.†

Certain correlations between the sizes of Ni, NiO, and CeO_2 crystallites, the unit cell parameter of CeO_2, and φ were found for the samples prepared using glycine (Fig. 5). The average size of CeO_2 crystallites ranges from 4.5 to 35 nm, NiO – from 4.7 to 29 nm, and Ni – from 4.8 to 19 nm, the maximum values of which are obtained at a stoichiometric ratio of glycine and oxidizer. Therefore, the smallest crystals in this study within the investigated range of fuel-to-oxidizer ratios are obtained at $\varphi < 1$ and $\varphi \geq 2$. The use of urea as fuel led to similar regularities; however, compared with glycine, the maximum crystallite size of CeO_2 was obtained at $\varphi = 2$ (Table S1†). Apparently additional studies are required to elucidate the general validity of these observations.

As described previously,[89] the crystallite growth occurs due to higher flame temperatures achieved in the reactions with higher fuel-to-oxidizer ratios. Subsequently, smaller crystallite sizes can be related to the increasing release of gases that remove heat from the reaction.[65] Because the amount of energy released during combustion depends on the initial fuel and reagents, as well as the resulting products, the maximum crystallite size can be obtained at various values of φ. For example, the dependence of the crystallite size on φ with an extremum close to 2 was previously shown for α-alumina,[90] $CuFe_2O_4$,[91] and $(Y_{1-m}Ce_m)_2SiO_5$.[92] Considering that the molar enthalpy of urea formation is less than that of glycine,[89] it can be supposed that the maximum temperature for urea is reached at a higher fuel-to-oxidizer ratio.

The cell parameter of CeO_2 at a glycine-to-oxidizer ratio of 1–1.6 turned out to be lower than 5.419 Å, which indicates the incorporation of nickel ions into the CeO_2 lattice and formation of a solid solution. In addition, lattice distortions may indicate the formation of new crystalline phases, including cerium nickelite.

The average sizes of crystallites of all phases turned out to be the largest for the samples containing the intense $CeNiO_3$ (111) reflection in the XRD pattern.

It has been proven that steam and aqueous phase reforming of alcohols are structure-sensitive reactions, *i.e.*, their rate, normalized to the number of exposed metal surface atoms, changes with the particle size.[93–95] However, there is no apparent agreement whether smaller of bigger particles are more beneficial for hydrogen production.[34,96,97]

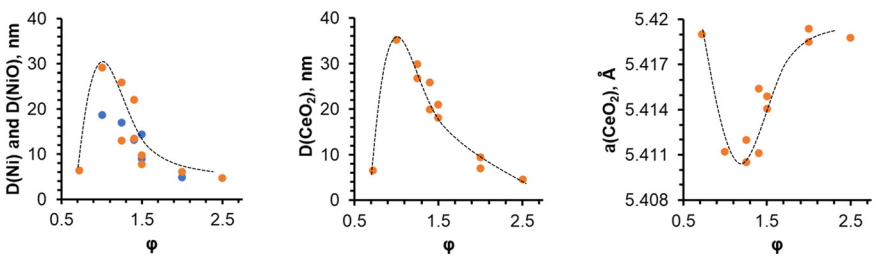

Fig. 5 Dependence of the Ni, NiO, and CeO_2 crystallite sizes and CeO_2 cell parameter on the fuel (glycine)-to-oxidizer ratio (φ). Blue dots correspond to nickel.

3.2. Ce–Co–O: synthesis features and phase composition

The synthesis of the cobalt-containing systems, as well as Ce–Ni–O, proceeds with a sparkling flame (Fig. 6, left). As a result, the powder is carried away from the reaction zone, especially at the stoichiometric fuel-to-oxidizer ratio (φ = 1). The abundant gas evolution leads to the formation of fluffy powders that are black at an increased fuel content (φ = 1.5–2). The obtained materials gain weight during heating in air (Fig. 6, left), with the largest weight gain obtained for φ = 2.

According to the XRD data, the obtained materials consist mainly of CoO and CeO_2 phases (Fig. 6, right). In addition, there are also XRD reflections related to Co and Co_3O_4. The data for the phase composition, the average crystallite size, and the CeO_2 unit cell parameter for Ce–Co oxide systems are given in Table 2.

The phase composition is also corrected for the increase in mass during heating, which corresponds to the oxidation of Co rather than CoO to Co_3O_4, because oxidation occurred between 145 and 310 °C,[98] and amorphous cobalt oxide based on the content of crystalline CoO, Co_3O_4, and metallic Co. With increasing fuel-to-oxidizer ratio, the fraction of both metal and amorphous cobalt oxide increases. In this case, the average size of CeO_2 crystallites decreases, while the lattice parameter increases. In general, for this system, as well as for Ce–Ni–O, the formation of solid solutions at φ = 1–1.5 is typical.

It is noteworthy that the size of the crystalline phases in the Ce–Ni–O and Ce–Co–O systems is approximately the same under the same experimental conditions, which can be explained by the close values of the formation enthalpies for metal nitrates. Compared to the data presented in ref. 99, where combustion of a mixture of cobalt nitrate and glycine was carried out, the crystallites of cobalt and cobalt oxides are smaller in size.

3.3. Structural and textural properties

According to SEM micrographs, the Ce–Ni- and Ce–Co-containing materials obtained by the SCS method using glycine as a fuel are identical and have a typical foamy structure (Fig. 7a–d). Unlike that of glycine, the morphology of the powders obtained by combustion with urea is represented by agglomerates consisting of rounded aggregates (Fig. 7e and f). The formation of such agglomerates for a Ni–CeO_2 system was also achieved in ref. 31 and 71. It was found that glycine, being able to interact very well with metal cations, led to more intense combustion, giving a branched wool structure with softer agglomerates compared to urea during the preparation of nickel oxide powders.[79] The data for the elemental composition indicate an excess of nickel with respect to cerium (Ni : Ce (N. 3-2) = 53.5 : 46.5 at%), which means a slight deviation of the nickel oxide content from the targeted one (*ca.* 32.9 wt% instead of 30%). Based on the arithmetic average content of nickel oxide in four samples (Table S2†), 33 wt% NiO was taken for calculations of the phase composition.

The results of studying the porous structure of the as-prepared samples are shown in Fig. S2† and Table 3. With increasing φ, the specific surface area for the Ce–Ni–O systems varies from 8 to 43 $m^2\ g^{-1}$ with a minimum at φ = 1, and the pore size changes from 13 to 54 nm with a maximum for the same sample. The observed effect can be explained by the influence of the CeO_2 crystallite size, which decreases proportionally with the increase in the specific surface area. The porous characteristics for Ni- and Co-containing systems with the highest content of the amorphous phase (φ = 2*) turned out to be identical. The specific surface area of these systems is *ca.* 26 and 20 $m^2\ g^{-1}$, respectively, with a total pore volume of 0.1 $cm^3\ g^{-1}$ and an average pore diameter of 13–15 nm.

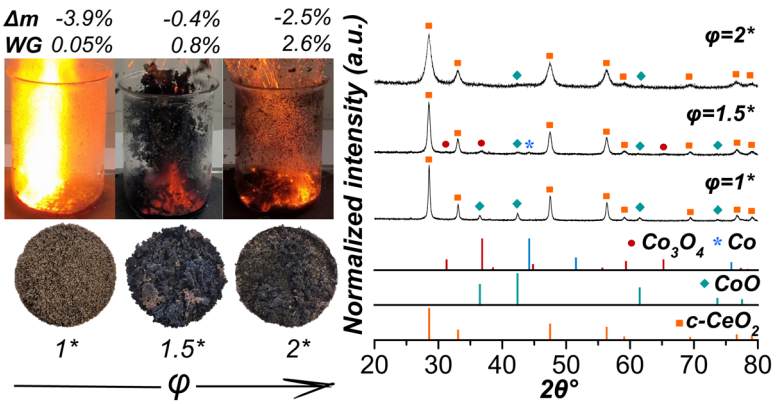

Fig. 6 The glycine–nitrate solution combustion synthesis and macromorphology of the Ce–Co–O systems obtained at various fuel-to-oxidizer ratios and with covering (left, where Δm and WG – the total weight change and the weight gain, respectively). XRD patterns of Ce–Co oxide systems obtained by combustion of glycine–nitrate solutions at different fuel-to-oxidizer ratios (right, where c-CeO_2 – cubic ceria (JCPDS card no. 01-075-8371); Co_3O_4 – JCPDS card no. 00-042-1467; CoO – JCPDS card no. 00-048-1719; Co – JCPDS card no. 00-015-0806).

Table 2 Data for the phase composition and crystallinity of the synthesized Ce–Co–O systems with covering

	Phase composition according to Rietveld/corrected,[a] wt%										
φ	CeO_2	CoO	Co_3O_4	Am. Co oxide[b]	Co	Co (TGA),[c] wt%	$D(CeO_2)$, nm	$a(CeO_2)$, Å	D(CoO), nm	$D(Co_3O_4)$, nm	D(Co), nm
1	73/67	27/27	0/0	6	0/0	0.1	24.0	5.4094	28.1	0	0
1.5	72/67	8/8	14/14	9	6/2	2.1	21.1	5.4119	10.6	8.9	8.2
2	100/67	0/0	0/0	26	0/7	7.2	9.8	5.4161	—	0	—

Note: [a] Taking into account amorphous cobalt oxide and TGA results. [b] The amount of amorphous cobalt oxide is equal to the difference between the total amount (according to stoichiometry, no more than 33 wt%) and crystalline cobalt oxide (determined by the Rietveld method) with metallic Co. [c] Calculated from the weight gain of the sample during heating, equal to the mass of oxygen involved in the oxidation of cobalt according to the equation $3Co + 2O_2 = Co_3O_4$; φ is the fuel-to-oxidizer ratio; the ratio of the weighted (R_{wp}) and expected (R_e) R-factors was 0.97–0.98, which characterizes the goodness of fit (if the squared value is equal to one or constant, the refinement procedure is completed); "—" not possible to determine using the Rietveld refinement.

According to ref. 31, amorphous oxides of Ni and Co can fill the intergranular space of CeO_2, thereby blocking small pores with the largest surface.

The characteristics of the systems obtained in this study were compared with the characteristics of Ni/CeO_2 previously synthesized by the solution combustion synthesis method (Table 3).

As can be seen, almost all samples differ primarily in nickel content. It was found that the samples prepared in this study at φ = 0.72 and 2*, the most dispersed phases of ceria and nickel, have the highest nickel content and the largest specific surface area among the Ni–CeO_2 systems synthesized with glycine without additives. NaCl acts as a diluent and reduces the combustion temperature,[89] resulting in an increase in the specific surface area and a decrease in the particle and crystallite sizes even for a highly loaded Ni-based system.[67] However, in this case, sodium and chlorine impurities remain in the catalyst, requiring washing.

In the case of urea, the stoichiometric combustion (φ = 0.95–1) mainly leads to a highly developed specific surface area and a small crystallite size at a low nickel content (up to 10 wt%). Other less often used fuels (oxalyldihydrazide, glycerol, carbohydrazide,[71] hydrous hydrazine[70]) result in worse textural properties of the materials.

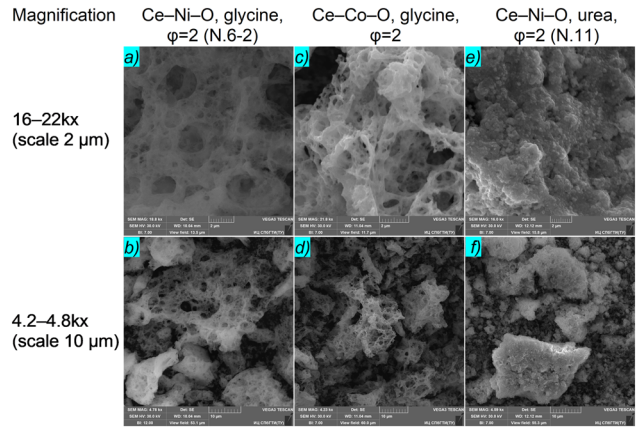

Fig. 7 SEM micrographs of Ce–Ni(Co)–O systems obtained by the SCS method using different fuels (with covering).

3.4. Reducibility

Various forms of Ni^{2+} compounds, the sequence of their reduction, and the interaction type between the metal and CeO_2 were determined by H_2-TPR. Fig. 8a shows the reduction curves for the Ce–Ni oxide systems obtained at various fuel-to-oxidizer ratios, as well as with and without covering. With increasing φ, the main reduction peak shifts towards lower temperatures, which is explained by an increase in the fraction of amorphous NiO (compared to crystalline), a decrease in the degree of interaction between NiO and CeO_2 particles, or an average crystallite size. It is known from previous studies[31] that amorphous NiO is distributed in voids between CeO_2 agglomerates, subsequently exhibiting poor self-interaction. The peak α shown in Fig. 8a can correspond to the reduction of amorphous nickel oxide, with an increase in the amount of which shifting the peak towards higher temperatures, while the β peak can be attributed to the reduction of fine NiO particles distributed over the CeO_2 surface and is characterized by increased interactions with CeO_2.

At a stoichiometric fuel-to-oxidizer ratio, the largest NiO crystallites and a $CeO_2(Ni^{2+})$ solid solution are obtained, whose reduction is difficult from the topochemical point of view and occurs at high temperatures (γ and ε peaks, respectively). The high-temperature δ-peaks for the samples obtained at φ = 0.72 and 2 can be explained by the strong interactions of nickel nanoparticles with the ceria surface. Some examples of TPR data modelling assuming the presence of different nickel oxide species are presented in Fig. S3 and Table S3.† Ceria is also reduced in the process, as evidenced by the ratio of the amount of consumed hydrogen to metal (mol H_2 per mol Ni, Table S4†) exceeding unity.

Fig. 8b shows the reduction curves for the Ce–Co oxide systems, whose behavior is similar to those of the Ni-containing systems. With increasing φ, the peaks shift towards lower temperatures due to an increase in the amorphous cobalt oxide fraction, a decrease in the interactions between CeO_2 and cobalt oxide, and the average size of crystallites. The peaks at 295–334 °C can be associated with the reduction of amorphous cobalt oxide, as well as

Table 3 Comparison of physical and textural characteristics for Ni–CeO_2 systems prepared by the combustion synthesis method

Fuel, additive, φ	Ni, wt%	S_{BET} ($m^2\ g^{-1}$)/$\sum V_p$ ($cm^3\ g^{-1}$)/d_p (nm)	D(Ni), nm	D(CeO_2), nm	Method[c]	Ref.
Glycine, 0.72	26.3	43/0.24/22.5	—	6.5	XRD	This work
Glycine, 1	26.3	8/0.11/53.7	18.7	35.2	XRD	This work
Glycine, 2*	26.7	26/0.09/13.3	4.8	9.5	XRD	This work
Glycine, NaCl, 1–1.1	46.3	77/0.18/9.9	7.2[a]	11.2[a]	XRD	67
Glycine, 1	15.1	21/0.06/12.6	19.2[a]	10.4	XRD/CO chemisorption	100
Glycine, 2	5.8	12/—/13.2	16.2[a]	—	TEM	70
Glycine, 0.7	5.4	7/0.05/—	22.3[a]	40.8[a]	XRD	68
Urea, 0.95	2.25–2.34	72/0.05/3.0	2.4[a]	10.8	XRD/TEM	31
Urea, 0.95	8.46–8.71	73/0.05/3.0	—	9.5	XRD	31
Urea, 1[d]	7.8	49/—/—	5.5[b]	8.6	XRD	71
Urea, 1	7.8	14/—/—	5.6[b]	12.9	XRD	71
Urea, 1	19.6	<10/0.01/18.5	18.8 ± 1[a]	—	XRD	29
Hydrous hydrazine, 0.5	5.8	12/—/14.8	10.3[a]	—	TEM	70
Hydrous hydrazine, 2	23.6	14/—/15.2	23.1–23.9[a]	—	XRD/TEM	70

Note: [a] After reduction. [b] For NiO. [c] Determination method of crystallite sizes. [d] Instead of cerium nitrate, ammonium cerium nitrate was used.

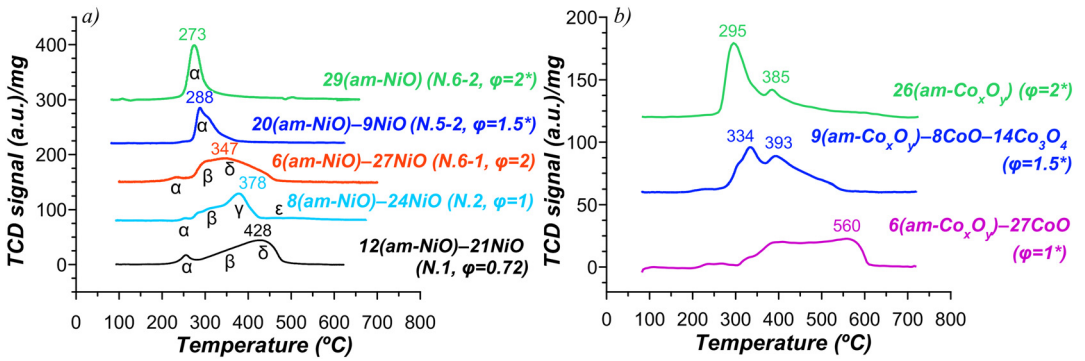

Fig. 8 H_2-TPR curves of the Ce–Ni–O (a) and Ce–Co–O (b) systems, obtained by the SCS method at various fuel-to-oxidizer ratios (φ).

Co^{3+} at the contact point between Co_3O_4 and CeO_2.[101] According to the literature,[102] large Co_3O_4 crystallites are often reduced to Co^0 in one stage. Therefore, the peaks at 385–393 °C can be attributed to both the reduction of CoO particles, formed due to the reduction of Co_3O_4, and bulk CoO, which weakly interacts with CeO_2.

The reduction of the largest CoO crystallites obtained at φ = 1 is difficult and occurs at higher temperatures. In addition, in this case, the reduction profile consists of peaks that have merged into one, which can be explained by the strong interactions of cobalt particles with the surface of cerium oxide. It is also known that cobalt ions can improve the reduction of bulk oxygen CeO_2,[103] which usually occurs at 800 °C. This phenomenon is interpreted as the transition of hydrogen from cobalt to cerium. The same promoting effect of cerium reduction was reported in the literature.[104]

Thus, the results of H_2-TPR indicate that the most reactive, easily reduced oxides of Co and Ni, which act as active components in many heterogeneous catalytic processes, are obtained with an excess of fuel and covering with a Petri dish after completing combustion to minimize the interactions of solid products with oxygen.

3.5. Chemisorption properties and defectiveness of CeO_2

The chemisorption properties and dispersion for various Ce–Ni–O systems were measured using H_2- and CO_2-TPD. The choice of Ni-containing systems instead of Ce–Co–O is due to a wide variety of conditions for their preparation. Similar dependencies can be expected for both of these systems.

The spectra show a broad asymmetric H_2 desorption peak resulting from the overlap of signals from metal particles of different diameters, surfaces, or positions (Fig. S4†). The Ce–Ni–O system obtained at stoichiometric φ has the smallest area of low-temperature peaks (<250 °C) associated with H_2 weakly chemisorbed on the surface due to highly dispersed Ni and defects. Thus, the highest defect density of the samples can be expected with a deficit and excess of fuel (φ = 0.72 and 2). At the same time, at φ = 0.72, despite the high specific surface area, the dispersion (D) and specific metal surface area (A) are lower than those at φ = 2 (Table 4), which can be explained by the influence of the synthesis conditions. Furthermore, Raman spectroscopy was carried out to identify the differences in defectiveness.

Basic catalyst sites play an important role in the reaction pathways and selectivity during GSR, facilitating the

Table 4 Chemisorption and Raman results for the Ni–Ce–O systems prepared at various φ values

φ	H_2, μmol g^{-1}	D, %	A, m^2 per g Ni	d, nm	SDs/F_{2g}	D2/F_{2g}	D3/F_{2g}	μmol CO_2 per g[a]
0.72	129.4	5.7	38.2	17.6	0.31	1.55	1.89	199
1	47.0	2.1	14.0	48.2	0.00	0.19	0.36	52
2	152.8	6.8	45.5	14.8	0.06	0.95	1.63	n/d
2*	156.3	6.9	45.9	14.7	0.00	1.04	1.33	261

Note: [a] According to CO_2-TPD; D – dispersion; A – metal specific surface area; d – metal diameter; SDs – surface defects; D2 – extrinsic defects; D3 – oxygen vacancies; n/d – no data.

adsorption of CO_2 generated during steam reforming of glycerol. According to CO_2-TPD, the amount of adsorbed CO_2 on the surface of reduced Ni–Ce–O catalysts depends substantially on φ with a minimum at φ = 1 (Table 4).

Raman spectra of the as-prepared Ce–Ni–O systems are presented in Fig. 9. It should be noted that the studied samples are generally homogeneous, but large particles (10–20 μm) are visible by optical microscopy. They have also been studied at several random points and their spectra are well reproduced (Fig. S5†). Each spectrum contains an intense band at 462 ± 2 cm^{-1} associated with the F_{2g} mode (triply degenerate) of CeO_2. According to ref. 105, the F_{2g} band belongs to the symmetrical stretching vibration of CeO_8 units.

In addition, for all samples, the D band phonon (or LO mode) in the region of 500–700 cm^{-1} is observed, indicating the presence of CeO_2 bulk defects, which can be divided into three bands: 591 ± 2 (D1, Fig. 9, red area), 631 ± 2 (D2, Fig. 9, yellow area), and 553–554 (D3, Fig. 9, blue area). According to ref. 106, the D1 band is attributed to "internal" defects already present in pure ceria, for example, a Frenkel type oxygen vacancy generated by the migration of oxygen anions from tetrahedral sites to octahedral sites. The D2 band is related to "external" defects generated by the Ni addition, while the third component (D3) is usually assigned to oxygen vacancies associated with the presence of Ce^{3+} cations. The spectra also show broad signals from NiO at 419–424 cm^{-1} (TO mode) and 509–516 cm^{-1} (LO mode).[107,108]

It was found that only two samples (φ = 0.72 and 2) had Raman bands at *ca.* 224 cm^{-1}, which is associated with surface defects (SDs), namely, the Ce–OH vibration.[105] As noted in ref. 105, the highest intensity of this peak is observed for samples with smaller crystals and a larger specific surface area.

The defect amount in the four samples was estimated by calculating the ratios between the area of the bulk (D2, D3) or surface defects (SDs) and the F_{2g} mode; these parameters, called D1/F_{2g}, D2/F_{2g}, and SDs/F_{2g}, respectively, are summarized in Table 4. The obtained data confirm that a fuel deficiency and excess contribute to the formation of both bulk and surface defects. At the same time, for the sample obtained at φ = 2* (with covering), no surface defects were found, which can be explained by the presence of surface metal particles.

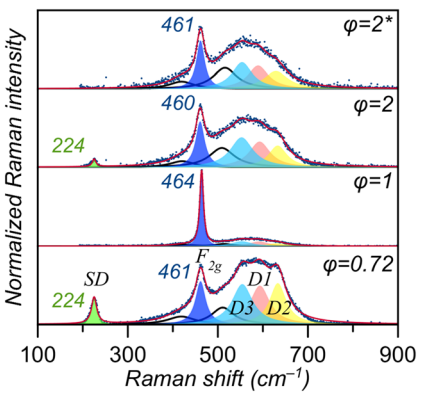

Fig. 9 Raman spectra with deconvolution for Ce–Ni–O systems prepared at different φ values.

3.6. Activity in GSR

The initial screening of the catalysts was performed in glycerol steam reforming, which is due to the simplicity, as well as the possibility of selecting the most efficient catalysts for their subsequent study in glycerol aqueous-phase reforming. The samples that differ significantly in the dispersity and amorphization of the phases were selected. The same fuel (glycine) for synthesis was chosen to compare the different catalytic systems. Fig. 10a and b show the data for hydrogen yield as a function of time-on-stream for the selected compositions.

In terms of hydrogen yield, the nickel systems are more active than the cobalt systems. Both systems are characterized by the following general trends: the samples with the highest initial activity (time-on-stream of 15 min) undergo rapid deactivation in the first hour of testing. For them, in general, a higher value of the deactivation constant is obtained (Fig. 10a and b). This is explained by the partial encapsulation by carbonaceous deposits of metal Ni and Co nanoparticles localized on the surface and between CeO_x aggregates.[21] The lack of contact between the metal particles and the defective support, as well as the low process temperature, makes it difficult to remove coke during the reaction with steam. It should be noted that catalysts with this feature are characterized by increased residual activity (Fig. 10b, time-on-stream is more than 1 h), which exceeds the residual activity of the other systems studied in this work.

Comparison of systems in terms of the hydrogen formation rate $r(H_2)$, at which the influence of the

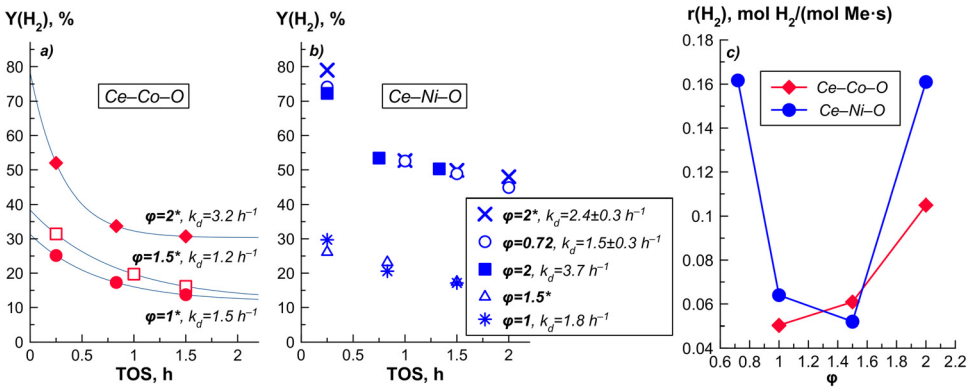

Fig. 10 Hydrogen yield *versus* time-on-stream for Co- (a) and Ni-containing (b) systems; and dependence of the rate of hydrogen formation on the glycine-to-oxidizer ratio (c). Conditions: m_{cat} = 40 mg, V_{lq}(water + glycerol) = 7.3–7.9 mL h^{-1}, $V(N_2)$ = 30 mL min^{-1}, T = 520 °C. Because of a limited number of data points, the statistical analysis of the parameters, determined using eqn (10), was reliable just only in a few cases indicated by errors for the corresponding constants. In other cases, an exact approximation of the experimental points did not allow determination of the parameter errors.

deactivation is minimal, shows its extreme dependence on φ (Fig. 10c) with minima at φ = 1 and 1.5. Results in the Co–Ni series are in line with the experimental and theoretical work on methane steam reforming.[109] Namely an increase of activity depending on the metal can be related to the energy of oxygen adsorption on the surface.

The highest initial rate of hydrogen formation was shown by those Ce–Ni–O and Ce–Co–O systems, which are characterized by a high dispersion of Ni and Co nanoparticles, which is provided by moderate combustion conditions with a deficit or excess of fuel ($\varphi < 1$ and $\varphi \geq 2$), and the increased dispersion and defectiveness of CeO_2 in combination with an increased specific surface area. At the same time, the Ce–Ni(Co)–O samples with a large crystallite size (φ = 1–1.5) are characterized by a low initial hydrogen formation rate, including the Ce–Ni–O sample obtained at φ = 1 containing the largest amount of perovskite o-$CeNiO_3$.

The experiments also showed that the covering that prevents the oxidation of fine Ni particles makes it possible to exclude the reductive activation stage of the sample with hydrogen directly in the catalytic reactor before testing without a loss of activity and stability.

The Ce–Ni–O systems obtained at φ = 0.72, 2, and 2* have a hydrogen yield close to the highest thermodynamically possible value for these conditions (88.5% or 6.2 mol mol^{-1}). The calculation of the Mears and Weisz–Prater criteria demonstrated that during experiments, there were no internal and external diffusion limitations. To establish the maximum productivity of these samples, additional experiments were carried out with a lower catalyst loading, as well as a high flow of the feedstock. Fig. S6† shows the yield of glycerol to gaseous products and the integral rates of hydrogen formation $r(H_2)$ and glycerol transformation r(gly) as a function of WHSV. The rates have been calculated at 4 min of time on stream, and thus the dependence of the integral rates on WHSV is related to a non-zero order reaction rather than deactivation. Subsequently, the turnover frequency (TOF) was calculated, showing an increase of TOF in the presence of surface defects (Table 5), which is consistent with the literature.

The surface anion vacancies of CeO_2 are the activation sites for additional water molecules involved in the catalytic cycle. TOF_{Gly} was also found to increase with increasing Ni particle size at a constant Ni content. Similar regularities were obtained in ref. 42 and 96. These results suggest that

Table 5 Comparison of TOF values for catalysts obtained in this work and presented in the literature

Catalyst	Synthesis method	Ni loading, wt%	$d(Ni)_{XRD\ or\ TEM}$, nm	$d(Ni)_{Chem}$, nm	SDs/F_{2g}	T, °C	TOF_{H_2}, s^{-1}		TOF_{gly}, s^{-1}	
							2500 h^{-1}	60 h^{-1}	2500 h^{-1}	40–60 h^{-1}
Ni/CeO_2 φ = 0.72	SCS	26.3	6.4 (NiO)	17.6	0.31	520	10.9	1.4	2.1	0.33
Ni/CeO_2 φ = 2	SCS	26.3	6.1 (NiO)	14.8	0.06	520	11.5	1.4	2.1	0.19
Ni/CeO_2 φ = 2*	SCS	26.7	4.8	14.7	0.00	520	9.0	1.1	1.7	0.26
Ni/CeO_2 (ref. 31)	SCS	6.8	2.6	—	0.47	550	—	—	—	0.06
Ni/CeO_2 (ref. 22)	WI	11.6	—	16.5	—	600	—	—	—	0.31

Note: SCS – solution combustion synthesis; WI – wet impregnation; $d(Ni)_{XRD\ or\ TEM}$ – the mean diameter of Ni particles calculated from XRD or TEM; $d(Ni)_{Chem}$ – the mean diameter of Ni particles calculated from chemisorption data; SDs – surface defects (Table 4).

steam reforming is a structure sensitive reaction. Comparison of TOF values shows that the catalysts obtained in this work have the highest values among other Ni/CeO_2 systems (Table 5 and data presented in ref. 31). These values are obtained at a relatively low reforming temperature.

3.7. Selectivity in GSR

The series of performed tests also made it possible to compare the synthesized systems in terms of selectivity to the main (H_2, CO_2, CO) and side (C_1–C_3 hydrocarbons) reaction products. The specified selectivity values do not take into account coke formation. Systems containing Ni and Co are generally characterized by a positive slope of the $S(H_2)$–X_{Ggas} dependence (Fig. 11a), which corresponds to the consecutive reactions of H_2 formation. A simultaneous decrease of $S(H_2)$ and X_{Ggas} is associated with a lower contribution of WGS or an increase in the reverse WGS (RWGS, $CO + H_2O \leftrightarrow CO_2 + H_2$). This is also evidenced by a decrease in $S(CO)$ and an increase in $S(CO_2)$ with elevation of X_{Ggas} (Fig. 11b and c). Extrapolation of $S(CO_2)$ and $S(CO)$ to close to zero glycerol conversion shows that these products are formed directly from glycerol as a result of two different reactions – steam reforming and thermal decomposition, respectively:[110]

$$C_3H_8O_3 + 3H_2O = 3CO_2 + 7H_2,\ \Delta G^0_{298} = -48.85\ \text{kJ mol}^{-1} \quad (13)$$

$$C_3H_8O_3 = 3CO + 4H_2,\ \Delta G^0_{298} = 37.04\ \text{kJ mol}^{-1} \quad (14)$$

The most active Ce–Ni–O catalysts exhibited a higher $S(CO_2)$ and, correspondingly, a lower $S(CO)$ at the same X_{Ggas} compared to Ce–Co–O. Therefore, the Ce–Ni–O systems obtained at φ = 0.72 and 2 make it possible to achieve the highest H_2/CO ratio (Fig. 11e), closest to the stoichiometric one, with complete conversion of glycerol into CO_2 and H_2 (H_2/CO_2 = 2.33, Fig. 11d). For these Ce–Ni–O systems (φ = 0.72 and 2), an increased basicity is observed, which affects CO_2 adsorption and, consequently, the H_2/CO_2 ratio. However, in addition to basicity, with a change in φ, other properties also change, such as defectiveness, dispersion, and crystallite size, affecting the activity and selectivity. Therefore, the selectivity cannot be attributed solely to basicity.

There is a very small amount of data in the literature for steam glycerol reforming on cobalt–ceria systems. All available results of the activity of various cobalt-based systems are presented in Table 6. Reaction conditions significantly affect activity and selectivity. The experimental conditions closest to those in this work were used in ref. 111 for $15Co/Al_2O_3$, which demonstrated a significantly low glycerol conversion into gaseous products and H_2 selectivity compared to $26.3Co/CeO_2$ synthesized by SCS. Data comparison at approximately the same reaction temperature (500–525 °C) shows that 9.2 wt% Co on Ca–HTlc has a higher hydrogen yield due to lower WHSV.[116] However, the samples obtained in this work demonstrated a rather high activity and selectivity upon a nonproportional elevation of WHSV, pointing out a higher productivity.

For a more detailed understanding of the differences in the catalytic action of the synthesized systems, the S–X_{Ggas} dependencies for by-products were also analyzed (Fig. 12). The presence of a slope in the graphs of S–X dependencies for ethane, ethylene, and propane indicates that they are formed directly from glycerol as a result of consecutive dehydration and hydrogenation reactions of intermediate products. The decrease in selectivity to C_2–C_3 products indicates the possible occurrence of their reforming as well, being apparently more prominent with increasing glycerol conversion. Ni-containing systems are characterized by the

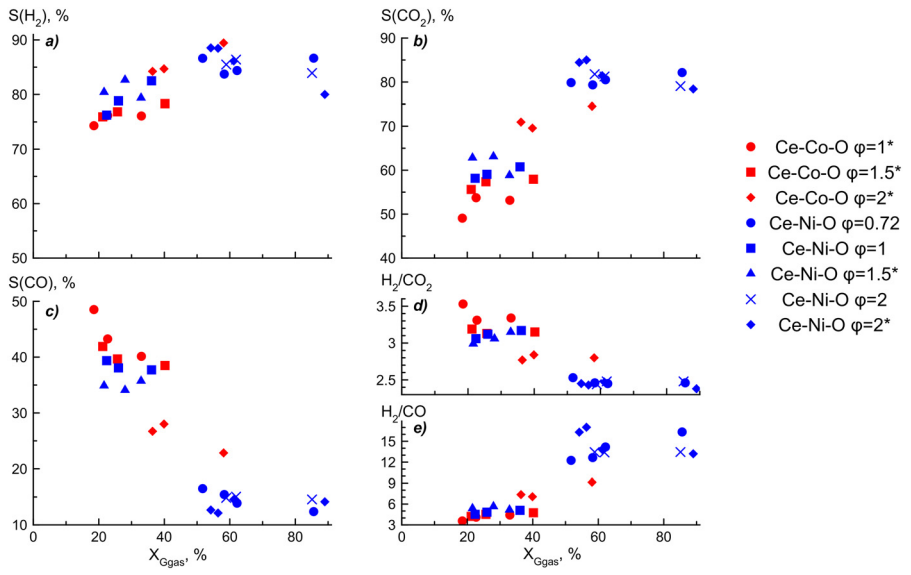

Fig. 11 Dependencies of selectivity to the main gaseous products (a–c), and H_2/CO_2 (d) and H_2/CO (e) ratios on glycerol conversion into gaseous products (X_{Ggas}). Conditions: m_{cat} = 40 mg, V_{lq}(water + glycerol) = 7.3–7.9 mL h^{-1}, $V(N_2)$ = 30 mL min^{-1}, T = 520 °C.

Table 6 Comparative data on the catalytic behavior of Co-containing catalysts obtained in this work and the literature

Ref.	Catalyst	Synthesis method	T, °C	WHSV, h^{-1}	TOS, min	X^*_{total} or X_{Ggas}, %	$Y(H_2)$, %	$S(H_2)$, %
50	$15Co/CeO_2$	WI	500	≈2.7	—	100*	—	92
111	$15Co/Al_2O_3$	WI	500	50 000[a]	—	≈12	≈77	≈64
112	10Co/YSZ	WI	525	6.45	230	94*[b]	53[b]	—
				10.8		87*[b]	36[b]	—
113	10Co/HAp	WI	650	≈22	60	92*	—	64
	10Co–10Ce/HAp					96*	—	63
114	7Co/SBA-15	WI	600	7.7	≈60/600	≈62*/56*	—	≈91/92
	7Co–8.5Ce/SBA-15				≈60/600	≈70*/64*	—	100/100
115	$La_{0.7}Ce_{0.3}CoO_3$	CP	500	≈5.1	60	≈90	≈51	≈56
116	9.2Co–Ca–HTlc	P	500	5600[a]	120	≈86*	≈86	—
117	5Ni–5Co/CNTs[c]	UWI	400	≈41	480	96*	—	87
This work	$26.3Co/CeO_2$	SCS, φ = 2*	520	197 (≈63 000[a])	15	58	52	89
					90	36	31	84

Note: [a] GHSV, mL g^{-1} h^{-1}. [b] Supercritical water reforming of glycerol at 25 MPa. [c] Ni and Co species in the cave of the support; "≈" – values were calculated from the data presented in the literature; WI – wetness impregnation; CP – co-precipitation; P – precipitation; UWI – ultrasonic wetness impregnation.

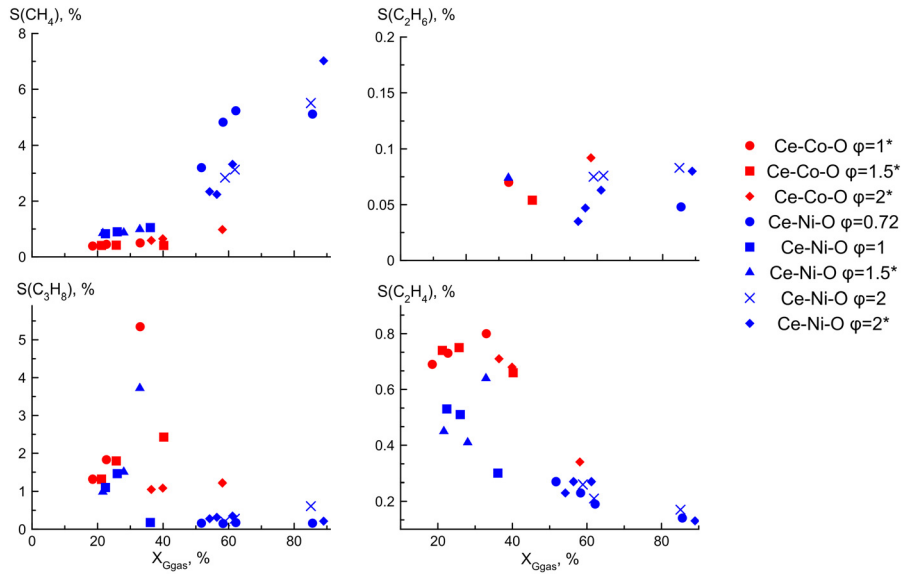

Fig. 12 Dependencies of selectivity to by-products on glycerol conversion into gaseous products.

lowest selectivity for these products. At the same time, for Ce–Ni–O (φ = 0.72 and 2), an increased $S(CH_4)$ is observed, which is apparently formed mainly as a result of CO and/or CO_2 hydrogenation. This is evidenced by a drop in $S(H_2)$ and $S(CO_2)$, a stop in the decrease in $S(CO)$ at $X_{Ggas} > 50\%$, and a growth of $S(H_2)$ at the same time to diminish $S(CH_4)$ and X_{Ggas}. Moreover, a non-zero $S(CH_4)$ for a near-zero X_{Ggas} indicates the existence of some additional route for the formation of methane directly from glycerol.

Based on the obtained results and the literature data,[42,118] a network of the main reactions in the gas phase can be proposed as shown in Fig. 13. The scheme is divided into three main paths of formation: (1) methane from glycerol and syngas or *via* RWGS; (2) C_2-gases from ethanol; (3) C_3-gases from 2-propanol.

The spent catalysts were examined by simultaneous thermal analysis (Fig. S7†) and XRD (Fig. S8†) to determine

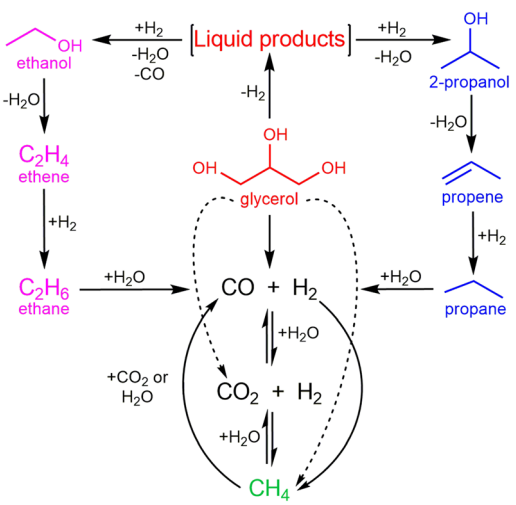

Fig. 13 The reaction network in GSR.

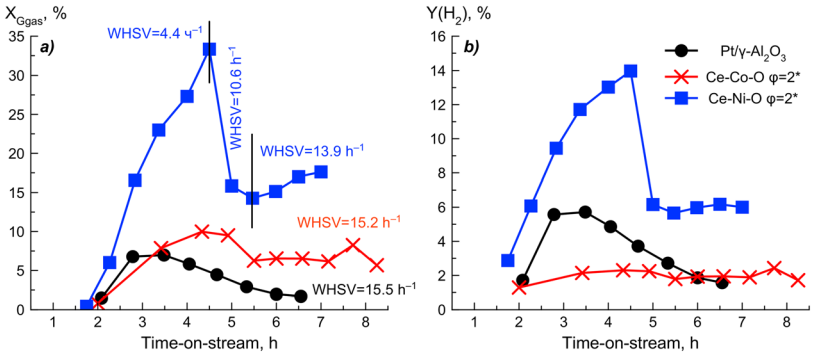

Fig. 14 Glycerol conversion into gaseous products (a) and hydrogen yield (b) over time-on-stream. Conditions for Pt-containing catalysts: T_{red} = 280 °C, m_{cat} = 200 mg, V_{lq} = 3 mL h^{-1}, WHSV = 15.5 h^{-1}. Conditions for Ce–Ni–O: T_{red} = 280 °C, m_{cat} = 668 mg, V_{lq} = 3, 7.2 mL h^{-1}, WHSV = 4.4, 10.6 h^{-1}; m_{cat} = 635 mg, V_{lq} = 9.8 mL h^{-1}, WHSV = 13.9 h^{-1}. Conditions for Ce–Co–O: T_{red} = 330 °C, m_{cat} = 635 mg, V_{lq} = 9.8 mL h^{-1}, WHSV = 15.2 h^{-1}.

the amount and type of coke deposits, as well as changes in the phase composition and crystallinity. The obtained thermograms for the Ce–Ni systems clearly show two exothermic peaks in the temperature ranges of 200–400 and 400–600 °C. The exothermic effect of nickel oxidation is also superimposed on the first peak, since an increase in mass occurs in this range. According to the literature,[119,120] amorphous coke burns up to 550 °C, while graphite-like and/or filiform coke burns out at higher temperatures. At the same time, the presence of amorphous coke is observed for almost all samples (except for Ce–Ni–O obtained at φ = 1.5*), and "heavy" coke is observed for samples with a high dispersion of Ni nanoparticles (φ = 0.72, 2, 2*), which is consistent with their highest activity in glycerol steam reforming. For the sample obtained at φ = 0.72, the highest content of coke was observed due to a higher specific surface area. At the same time, according to the hydrogen yield, the maximum coke formation was not reached for all samples, since there was no sharp activity drop depending on TOS (Fig. 10). The exo-effects of the oxidation of Co and CoO are observed for all spent Ce–Co samples, except for Ce–Co at φ = 2, for which amorphous coke burns out at 277 °C.

XRD patterns of the spent catalytic systems (Fig. S8†) indicate the transition of cobalt and nickel oxides to a metallic form, which, as a rule, do not undergo strong enlargement during testing (with the exception of the most amorphous systems), as well as maintaining the size of cerium oxide crystallites.

3.8. Activity and selectivity in GAPR

Based on the results obtained in the previous section, it was decided to conduct further studies of the most active Ce–Ni–O (φ = 2*) and Ce–Co–O (φ = 2*) systems and compare them with a platinum–alumina catalyst in aqueous-phase reforming of glycerol. Fig. 14 displays the glycerol conversion and the yield of hydrogen as a function of time-on-stream for the studied systems. In all cases, an increase in conversion was observed in the first 3–6 hours of testing, which is associated with the filling of the entire system with generated gaseous products and a large set-up volume (a separator volume of 100 mL). A similar effect was observed in ref. 74.

It was found that the Ce–Ni–O system displays a significantly higher glycerol conversion and hydrogen yield compared to Pt/Al_2O_3. In general, the activity of the studied systems during aqueous-phase reforming increases in the same order as that during steam reforming of glycerol, namely: Co < Ni. A feature of Ce–Co–O compared to Ce–Ni–O, as well as Pt/Al_2O_3, is a low hydrogen yield at a relatively high conversion of glycerol into gaseous products. The Ce–Ni-containing system makes it possible to achieve a hydrogen yield comparable to that of Pt/Al_2O_3 at a close WHSV = 13.9–15.5 h^{-1} without undergoing significant deactivation. In addition, this sample does not reach the maximum rate of hydrogen formation at T = 231 °C (Fig. 15).

Additional information about the process, as well as on differences between the systems, is provided by the analysis of the S–X_{Ggas} dependencies (Fig. 16): as a general trend, a higher conversion (catalyst activity) at a close WHSV = 13.9–15.5 h^{-1} leads to more prominent side reactions: RWGS and CO and/or CO_2 methanation. This is evidenced by the increase of S(CO) and $S(CH_4)$ (Fig. 16c and d), the decrease in $S(H_2)$ and $S(CO_2)$ (Fig. 16a and b), and the H_2/CO ratio (Fig. 16e). In this case, the direct reaction of glycerol with

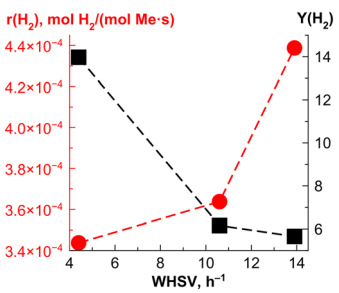

Fig. 15 Dependence of the H_2 formation rate and hydrogen yield on the WHSV of the glycerol–water mixture for the Ce–Ni–O sample (φ = 2*).

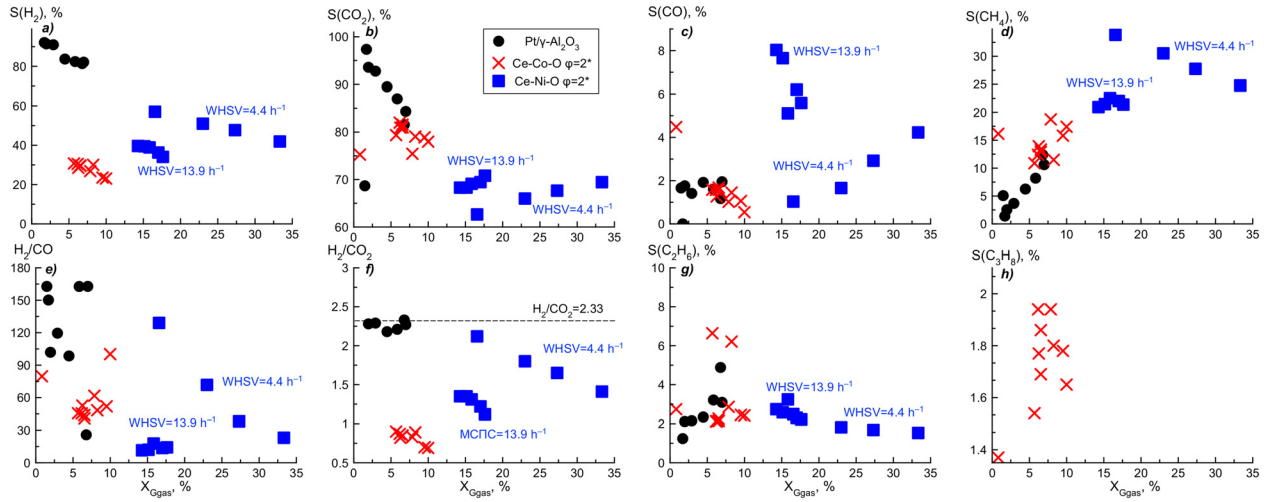

Fig. 16 Dependence of selectivity for all gas reaction products (a–d, g and h) and H_2/CO (e) and H_2/CO_2 (f) ratios on glycerol conversion into gaseous products.

water with the formation of H_2 and CO_2 ($S(CO_2)$ → 100%, $S(CO)$ → 0% at X_{Ggas} → 0%) prevails, in contrast to glycerol steam reforming. The different character of the S–X_{Ggas} dependencies during testing of Ce–Ni–O with a lower WHSV = 4.4 h^{-1} is apparently associated with the non-stationary composition of the gas mixture at the outlet due to the filling of the setup volume with the gaseous products.

The presence of methane, ethane, and propane in the reaction products causes a lower H_2/CO_2 ratio (Fig. 16f) for the Ce–Ni–O and Ce–Co–O catalysts compared to the stoichiometric one due to the occurrence of side reactions of dehydration, including liquid products, and subsequent hydrogenation.[42,121] The systems under study are characterized by a higher selectivity to C_2 hydrocarbons in GAPR compared to that in GSR (Fig. 16g and 12), which is related to the occurrence of decarbonylation leading to additional formation of CO from the liquid products of glycerol dehydrogenation.[42] A high selectivity to propane for Ce–Co–O in combination with a low $S(H_2)$ and H_2/CO_2 ratio due to hydrogenation of propene explains the lower hydrogen yield with an increased glycerol conversion into gaseous products (Fig. 16). It should also be noted that the increased selectivity to methane and C_2 hydrocarbons for Ce–Ni–O and Ce–Co–O, obtained in glycerol steam reforming, was also seen in aqueous-phase reforming. It additionally shows the similarity of these processes.

The selected test conditions – temperature, pressure, and WHSV, made it possible to compare the catalyst performance with those in the literature (Table 7), which for the Ce–Ni–O sample (φ = 2*) was similar to or even surpassed those for some nickel catalysts prepared by precipitation or impregnation in glycerol conversion into gaseous products, the H_2 yield and the rate of hydrogen formation, as well as selectivity to H_2 and CO_2. Such a result is ensured by both the

Table 7 Comparison of the catalyst behavior of Ce–Ni–O (φ = 2*) in GAPR with literature data

	This work		122	30	123	124
Synthesis method	Ce–Ni–O (φ = 2*), SCS		Ni/MgAl (hydrotalcite), co-precipitation	NiO/CeO_2, co-precipitation	Ni/γ-Al_2O_3, impregnation	$NiAl_2O_4$, co-precipitation
Ni^0, nm	4.8 (XRD)		12.0 (TEM)	5.3 (XRD)	—	12.0 (TEM)
Ni, wt%	26.7		23.0	14.9	20.0	42.3
Conditions						
T, °C	231		250	250	225	235
P, bar	34		35	20	23	35
WHSV, h^{-1}	4.4	13.9	5.0	5.0	4.0	24.5
Glycerol, wt%	10.0		7.8	15.0	10.0	10.0
Process indicators						
X_{Ggas}, %	33.3	17.6	≈16.0	17.3	≈44.0 (full)	≈27.0
$Y(H_2)$, %	14.0	6.0	10.1	—	—	≈8.1
$r(H_2)$, μmol mol^{-1} Ni per s	0.343	0.438	0.088	—	—	0.154
$S(H_2)$, %	41.9	39.6	31.7	95.7	≈42.0	≈35.0
$S(CO_2)$, %	69.5	68.3	72.5	56.1	—	55.9
$S(CO)$, %	4.2	8.0	3.5	36.8	—	1.70
$S(CH_4)$, %	24.8	20.9	24.1	7.1	—	42.4
H_2/CO_2	1.41	1.35	1.02	—	—	1.80

high dispersion of nickel compared to other systems, despite the high content of Ni, and interactions of Ni with CeO_x.

Conclusions

Currently, glycerol represents an emerging renewable bio-derived source that can be used to produce H_2 through steam (GSR) or aqueous-phase reforming (GAPR). A recent focus in catalytic reforming is improving catalysts and processes to maximize the catalyst lifetime and H_2 selectivity. For this purpose, in the present work, new Ce–Ni–O and Ce–Co–O catalytic systems (the content of Ni and Co, calculated as metal(II) oxides, is 30 wt%) were obtained and characterized. The synthesis was performed in one step by the SCS (solution combustion synthesis) method using different fuels and amounts relative to the oxidizing agents (φ = 0.7–3). Due to an increased and decreased glycine-to-oxidizer ratio ($\varphi < 1$; $\varphi \geq 2$), it was possible to avoid the formation of solid solutions characteristic of these systems and achieve the most dispersed phases, which is important, because glycerol reforming is a structure-sensitive reaction. It has been established for the first time that covering the beaker with a Petri dish immediately after the completion of the combustion makes it possible to retain a larger amount of the metal phase in the samples and to increase the fraction of amorphous Ni or Co oxides. Thus, by changing the fuel-to-oxidizer ratio and the excess of oxygen, various forms of Ni or Co and their interactions with CeO_2 were obtained, which affected the reduction sequence, defectiveness, porous characteristics, and chemical reactivity.

The synthesized materials were tested in glycerol steam reforming at atmospheric pressure and 520 °C. It has been shown that the Ce–Ni–O and Ce–Co–O systems characterized by a high crystallinity of phases (obtained at $\varphi < 1$ and $\varphi \geq 2$) have the highest activity and H_2 yield in GSR. The Ce–Ni–O systems, in contrast to Ce–Co–O, make it also possible to achieve the H_2/CO_2 ratio closest to the stoichiometric one (2.33) with complete conversion of glycerol into CO_2 and H_2. Prevention of the material oxidation during synthesis makes it possible to exclude the reductive activation stage of the samples before testing without a loss of activity and stability. On the other hand, according to Raman spectroscopy, this negatively affected the defective structure of cerium oxide.

Additional experiments carried out at increased WHSV for Ce–Ni–O, which was obtained with a fuel deficiency (φ = 0.72), resulted in a higher TOF due to a large number of surface defects. In addition, such a result can be associated with the largest Ni particle size among other systems according to H_2 chemisorption. However, in terms of the metal dispersion and the amount of coke deposits, this sample is inferior to the others.

The activity of the studied systems (obtained at φ = 2 without *a posteriori* oxidation) in aqueous-phase reforming of glycerol (34 bar, 231 °C) increased in the same order as that in GSR, namely, Co < Ni. With the Ni-containing system, it was possible to achieve a hydrogen yield comparable to that of Pt/γ-Al_2O_3 at a close WHSV without undergoing noticeable deactivation. The glycerol conversion into gaseous products, the yield and rate of hydrogen formation, and the selectivity to H_2 and CO_2 were also comparable.

In conclusion, the SCS-derived Ni/CeO_2 systems have significant potential as catalysts because of a variety of tunable textural and surface properties. Undoubtedly, further research is required to optimize the synthesis conditions for each specific case.

Author contributions

ANM – conceptualization, investigation, visualization, and writing – original draft. SOO – formal analysis, investigation, and visualization. MAG – investigation. ADT – investigation. JW – formal analysis. DYM – conceptualization and writing – review and editing.

Conflicts of interest

There are no conflicts to declare.

Acknowledgements

This research was funded by the Russian Science Foundation (grant number 22-23-20094, **https://rscf.ru/project/22-23-20094/**, accessed on 18 June 2023) and the St. Petersburg Science Foundation (agreement number 26/2022 from 14 April 2022). The authors would like to thank MSc Maria Chebanenko (Ioffe Institute) and MSc Maria Serazhim (St. Petersburg State Institute of Technology (Technical University)) for performing N_2 physisorption measurements.

Notes and references

1 A. G. Adeniyi and J. O. Ighalo, *Chem. Pap.*, 2019, **73**, 2619–2635.
2 P. J. Megía, A. J. Vizcaíno, J. A. Calles and A. Carrero, *Energy Fuels*, 2021, **35**, 16403–16415.
3 N. A. Roslan, S. Z. Abidin, A. Ideris and D. V. N. Vo, *Int. J. Hydrogen Energy*, 2020, **45**, 18466–18489.
4 A. Behr, J. Eilting, K. Irawadi, J. Leschinski and F. Lindner, *Green Chem.*, 2008, **10**, 13–30.
5 M. Anitha, S. K. Kamarudin and N. T. Kofli, *Chem. Eng. J.*, 2016, **295**, 119–130.
6 C. A. G. Quispe, C. J. R. Coronado and J. A. Carvalho, *Renewable Sustainable Energy Rev.*, 2013, **27**, 475–493.
7 Z. Pirzadi and F. Meshkani, *Fuel*, 2022, **329**, 125044.
8 A. Fasolini, D. Cespi, T. Tabanelli, R. Cucciniello and F. Cavani, *Catalysts*, 2019, **9**, 722.
9 R. R. Davda, J. W. Shabaker, G. W. Huber, R. D. Cortright and J. A. Dumesic, *Appl. Catal., B*, 2005, **56**, 171–186.
10 J. Chen, J. Sun and Y. Wang, *Ind. Eng. Chem. Res.*, 2017, **56**, 4627–4637.
11 K. N. Papageridis, G. Siakavelas, N. D. Charisiou, D. G. Avraam, L. Tzounis, K. Kousi and M. A. Goula, *Fuel Process. Technol.*, 2016, **152**, 156–175.

12 C. K. Cheng, S. Y. Foo and A. A. Adesina, *Catal. Today*, 2011, **178**, 25–33.
13 N. D. Charisiou, K. N. Papageridis, G. Siakavelas, L. Tzounis, K. Kousi, M. A. Baker, S. J. Hinder, V. Sebastian, K. Polychronopoulou and M. A. Goula, *Top. Catal.*, 2017, **60**, 1226–1250.
14 A. Bshish, Z. Yaakob, A. Ebshish and F. H. Alhasan, *J. Energy Resour. Technol.*, 2013, **136**, 012601.
15 T. Wang, H. Ma, L. Zeng, D. Li, H. Tian, S. Xiao and J. Gong, *Nanoscale*, 2016, **8**, 10177–10187.
16 O. Shtyka, Z. Dimitrova, R. Ciesielski, A. Kedziora, G. Mitukiewicz, J. Leyko, W. Maniukewicz, A. Czylkowska and T. Maniecki, *React. Kinet., Mech. Catal.*, 2021, **132**, 907–919.
17 S. Anil, S. Indraja, R. Singh, S. Appari and B. Roy, *Int. J. Hydrogen Energy*, 2022, **47**, 8177–8213.
18 M. L. Dieuzeide, M. Jobbagy and N. Amadeo, *Int. J. Hydrogen Energy*, 2014, **39**, 16976–16982.
19 E. A. Sanchez and R. A. Comelli, *Int. J. Hydrogen Energy*, 2014, **39**, 8650–8655.
20 C. Italiano, K. Bizkarra, V. L. Barrio, J. F. Cambra, L. Pino and A. Vita, *Int. J. Hydrogen Energy*, 2019, **44**, 14671–14682.
21 S. Adhikari, S. D. Fernando and A. Haryanto, *Renewable Energy*, 2008, **33**, 1097–1100.
22 S. Adhikari, S. D. Fernando, S. D. Filip To, R. Mark Bricka, P. H. Steele and A. Haryanto, *Energy Fuels*, 2008, **22**, 1220–1226.
23 K. K. Pant, R. Jain and S. Jain, *Korean J. Chem. Eng.*, 2011, **28**, 1859–1866.
24 E. V. Matus, A. S. Shlyakhtina, O. B. Sukhova, I. Z. Ismagilov, V. A. Ushakov, S. A. Yashnik, A. P. Nikitin, P. Bharali, M. A. Kerzhentsev and Z. R. Ismagilov, *Kinet. Catal.*, 2019, **60**, 221–230.
25 C. D. Dave and K. K. Pant, *Renewable Energy*, 2011, **36**, 3195–3202.
26 A. K. Seriyala, S. Appari and B. Roy, *Mater. Today: Proc.*, 2022, **76**(Part 2), 279–288.
27 A. K. Seriyala, A. Rao, C. Leclerc, S. Appari and B. Roy, *Int. J. Hydrogen Energy*, 2023, **48**, 15533–15554.
28 Y. Wang, S. Zhu, S. He, J. Lu, J. Liu, H. Lu, D. Song and Y. Luo, *Nanomaterials*, 2022, **12**, 816.
29 R. L. Manfro, A. F. Da Costa, N. F. P. Ribeiro and M. M. V. M. Souza, *Fuel Process. Technol.*, 2011, **92**, 330–335.
30 H.-J. Lee, G. S. Shin and Y.-C. Kim, *Korean J. Chem. Eng.*, 2015, **32**, 1267–1272.
31 Sh. O. Omarov, K. D. Martinson, A. N. Matveyeva, M. I. Chebanenko, V. N. Nevedomskiy and V. I. Popkov, *Fuel Process. Technol.*, 2022, **236**, 107429.
32 D. G. Araiza, A. Gómez-Cortés and G. Díaz, *Catal. Today*, 2020, **349**, 235–243.
33 F. Wang, L. Zhang, J. Deng, J. Zhang, B. Han, Y. Wang, Z. Li, H. Yu, W. Cai and Z. Deng, *Fuel Process. Technol.*, 2019, **193**, 94–101.
34 M. Greluk, W. Gac, M. Rotko, G. Słowik and S. Turczyniak-Surdacka, *J. Catal.*, 2021, **393**, 159–178.
35 B. Wang, Y. Xiong, Y. Han, J. Hong, Y. Zhang, J. Li, F. Jing and W. Chu, *Appl. Catal., B*, 2019, **249**, 257–265.
36 Y. Wang, S. Zhu, J. Lu, S. He, H. Lu, D. Song, D. Chen and Y. Luo, *Fuel Process. Technol.*, 2023, **243**, 107677.
37 M. Konsolakis, Z. Ioakimidis, T. Kraia and G. E. Marnellos, *Catalysts*, 2016, **6**, 39.
38 I. Rossetti, A. Gallo, V. DalSanto, C. L. Bianchi, V. Nichele, M. Signoretto, E. Finocchio, G. Ramis and A. di Michele, *ChemCatChem*, 2013, **5**, 294–306.
39 J. Vicente, J. Ereña, C. Montero, M. J. Azkoiti, J. Bilbao and A. G. Gayubo, *Int. J. Hydrogen Energy*, 2014, **39**, 18820–18834.
40 A. Carrero, J. A. Calles, L. García-Moreno and A. J. Vizcaíno, *Catalysts*, 2017, **7**, 55.
41 V. Nichele, M. Signoretto, F. Pinna, F. Menegazzo, I. Rossetti, G. Cruciani, G. Cerrato and A. Di Michele, *Appl. Catal., B*, 2014, **150–151**, 12–20.
42 Sh. O. Omarov, D. A. Sladkovskiy, K. D. Martinson, M. Peurla, A. Aho, D. Yu. Murzin and V. I. Popkov, *Appl. Catal., A*, 2021, **616**, 118098.
43 N. D. Charisiou, G. Siakavelas, L. Tzounis, B. Dou, V. Sebastian, S. J. Hinder, M. A. Baker, K. Polychronopoulou and M. A. Goula, *Int. J. Hydrogen Energy*, 2020, **45**, 10442–10460.
44 B. Jiang, L. Li, Z. Bian, Z. Li, Y. Sun, Z. Sun, D. Tang, S. Kawi, B. Dou and M. A. Goula, *Int. J. Hydrogen Energy*, 2018, **43**, 13200–13211.
45 Y. C. Sharma, A. Kumar, R. Prasad and S. N. Upadhyay, *Renewable Sustainable Energy Rev.*, 2017, **74**, 89–103.
46 D. L. Trimm, *Catal. Today*, 1997, **37**, 233–238.
47 Z. Xiao, Y. Li, F. Hou, C. Wu, L. Pan, J. Zou, L. Wang, X. Zhang, G. Liu and G. Li, *Appl. Catal., B*, 2019, **258**, 117940.
48 Z. Xiao, C. Wu, L. Wang, J. Xu, Q. Zheng, L. Pan, J. Zou, X. Zhang and G. Li, *Appl. Catal., B*, 2021, **286**, 119884.
49 M. D. Zhurka, A. A. Lemonidou and P. N. Kechagiopoulos, *Catal. Today*, 2021, **368**, 161–172.
50 B. Zhang, X. Tang, Y. Li, Y. Xu and W. Shen, *Int. J. Hydrogen Energy*, 2007, **32**, 2367–2373.
51 J. Llorca, N. Homs, J. Sales and P. Ramírez de la Piscina, *J. Catal.*, 2002, **209**, 306–317.
52 H. Song and U. S. Ozkan, *J. Catal.*, 2009, **261**, 66–74.
53 I. Ilgaz Soykal, H. Sohn and U. S. Ozkan, *ACS Catal.*, 2012, **2**, 2335–2348.
54 Zs. Ferencz, A. Erdőhelyi, K. Baán, A. Oszkó, L. Óvári, Z. Kónya, C. Papp, H.-P. Steinrück and J. Kiss, *ACS Catal.*, 2014, **4**, 1205–1218.
55 E. Varga, Z. Ferencz, A. Oszkó, A. Erdohelyi and J. Kiss, *J. Mol. Catal. A: Chem.*, 2015, **397**, 127–133.
56 M. Greluk, M. Rotko and S. Turczyniak-Surdacka, *Renewable Energy*, 2020, **155**, 378–395.
57 H. Wang, L. Zhang, M. Li, Y. Liu and X. Bai, *J. Rare Earths*, 2013, **31**, 565–571.
58 M. Greluk, M. Rotko, G. Słowik and S. Turczyniak-Surdacka, *J. Energy Inst.*, 2019, **92**, 222–238.
59 R. Li, C. Liu, L. Li, J. Xu, J. Ma, J. Ni, J. Yan, J. Han, Y. Pan, Y. Liu and L. Lu, *Fuel*, 2023, **336**, 126758.
60 C.-H. Yan, Z.-G. Yan, Y.-P. Du, J. Shen, C. Zhang and W. Feng, *Handbook on the Physics and Chemistry of Rare Earths*, 2011, vol. 41, pp. 275–472.

61 A. Cross, A. Kumar, E. E. Wolf and A. S. Mukasyan, *Ind. Eng. Chem. Res.*, 2012, **51**, 12004–12008.
62 A. Cross, S. Roslyakov, K. V. Manukyan, S. Rouvimov, A. S. Rogachev, D. Kovalev, E. E. Wolf and A. S. Mukasyan, *J. Phys. Chem. C*, 2014, **118**, 26191–26198.
63 A. Kumar, A. Cross, K. Manukyan, R. R. Bhosale, L. J. P. van den Broeke, J. T. Miller, A. S. Mukasyan and E. E. Wolf, *Chem. Eng. J.*, 2015, **278**, 46–54.
64 F. Deganello, *Mater. Today Proc.*, Elsevier Ltd, 2017, vol. 4, pp. 5507–5516.
65 F. Deganello and A. K. Tyagi, *Prog. Cryst. Growth Charact. Mater.*, 2018, **64**, 23–61.
66 B. D. Stojanovic, A. S. Dzunuzovic and N. I. Ilic, *Magnetic, Ferroelectric, and Multiferroic Metal Oxides*, Elsevier, 2018, pp. 333–359.
67 C. Han, Z. Cao, J. Yang, X. Lu, H. Liu, Z. Jin, Y. Zhang, S. Yang, X. Zheng and L. Wang, *Crystals*, 2022, **12**, 702.
68 C. Zhang, R. Zhang, H. Liu, Q. Wei, D. Gong, L. Mo, H. Tao, S. Cui and L. Wang, *Energies*, 2020, **13**, 5956.
69 L. Wang and H. Liu, *Catal. Today*, 2018, **316**, 155–161.
70 W. Kang and A. Varma, *Appl. Catal., B*, 2018, **220**, 409–416.
71 A. Vita, C. Italiano, C. Fabiano, M. Laganà and L. Pino, *Mater. Chem. Phys.*, 2015, **163**, 337–347.
72 A. N. Matveyeva, Sh. O. Omarov, M. A. Gavrilova, D. A. Sladkovskiy and D. Yu. Murzin, *Materials*, 2022, **15**, 7970.
73 S. L. González-Cortés and F. E. Imbert, *Appl. Catal., A*, 2013, **452**, 117–131.
74 N. Luo, X. Fu, F. Cao, T. Xiao and P. P. Edwards, *Fuel*, 2008, **87**, 3483–3489.
75 *Handbook of Heterogeneous Catalysis. 2nd Edition (Second, Completely Revised and Enlarged)*, ed. G. Ertl, H. Knözinger, F. Schüth and J. Weitkamp, Wiley-VCH, Weinheim, 2nd edn, 2008.
76 Sh. O. Omarov, E. A. Vlasov, D. A. Sladkovskiy, K. V. Semikin, A. N. Matveyeva, S. P. Fedorov, G. V. Oganesyan and D. Yu. Murzin, *Appl. Catal., B*, 2018, **230**, 246–259.
77 A. Kumar, E. E. Wolf and A. S. Mukasyan, *AIChE J.*, 2011, **57**, 2207–2214.
78 K. V. Manukyan, A. Cross, S. Roslyakov, S. Rouvimov, A. S. Rogachev, E. E. Wolf and A. S. Mukasyan, *J. Phys. Chem. C*, 2013, **117**, 24417–24427.
79 S. Hadke, M. T. Kalimila, S. Rathkanthiwar, S. Gour, R. Sonkusare and A. Ballal, *Ceram. Int.*, 2015, **41**, 14949–14957.
80 A. Khort, K. Podbolotov, R. Serrano-García and Y. K. Gun'ko, *J. Solid State Chem.*, 2017, **253**, 270–276.
81 X. Wang, M. Qin, F. Fang, B. Jia, H. Wu, X. Qu and A. A. Volinsky, *J. Alloys Compd.*, 2017, **719**, 288–295.
82 N. Ahmad, F. Alharthi, M. Alam, R. Wahab, S. Manoharadas and B. Alrayes, *Energies*, 2021, **14**, 2928.
83 M. P. Harikrishnan, A. J. C. Mary and A. C. Bose, *Electrochim. Acta*, 2020, **362**, 137095.
84 Q. Hu, B. Yue, H. Shao, F. Yang, J. Wang, Y. Wang and J. Liu, *J. Mater. Sci.*, 2020, **55**, 8421–8434.
85 J. Chen, Z. He, G. Li, T. An, H. Shi and Y. Li, *Appl. Catal., B*, 2017, **209**, 146–154.
86 H.-N. Barad, D. A. Keller, K. J. Rietwyk, A. Ginsburg, S. Tirosh, S. Meir, A. Y. Anderson and A. Zaban, *ACS Comb. Sci.*, 2018, **20**, 366–376.
87 N. Ahmad, R. Wahab, S. Manoharadas, B. F. Alrayes, M. Alam and F. A. Alharthi, *Molecules*, 2022, **27**, 356.
88 G. Sai Gautam, E. B. Stechel and E. A. Carter, *Chem. Mater.*, 2020, **32**, 9964–9982.
89 E. Novitskaya, J. P. Kelly, S. Bhaduri and O. A. Graeve, *Int. Mater. Rev.*, 2021, **66**, 188–214.
90 C.-C. Chen and K.-T. Huang, *J. Mater. Res.*, 2005, **20**, 424–431.
91 N. M. Deraz, *J. Alloys Compd.*, 2010, **501**, 317–325.
92 E. J. Bosze, J. McKittrick and G. A. Hirata, *Mater. Sci. Eng., B*, 2003, **97**, 265–274.
93 G. Pipitone, G. Zoppi, R. Pirone and S. Bensaid, *Int. J. Hydrogen Energy*, 2022, **47**, 151–180.
94 N. Palmeri, S. Cavallaro, V. Chiodo, S. Freni, F. Frusteri and J. C. J. Bart, *Int. J. Hydrogen Energy*, 2007, **32**, 3335–3342.
95 M. Boudart, *Adv. Catal.*, 1969, **20**, 153–166.
96 A. L. M. Da Silva, J. P. Den Breejen, L. V. Mattos, J. H. Bitter, K. P. De Jong and F. B. Noronha, *J. Catal.*, 2014, **318**, 67–74.
97 A. V. Kirilin, B. Hasse, A. V. Tokarev, L. M. Kustov, G. N. Baeva, G. O. Bragina, A. Yu. Stakheev, A.-R. Rautio, T. Salmi, B. J. M. Etzold, J.-P. Mikkola and D. Yu. Murzin, *Catal. Sci. Technol.*, 2014, **4**, 387–401.
98 A. S. Lozhkomoev, A. V. Pervikov, S. O. Kazantsev, K. V. Suliz, R. V. Veselovskiy, A. A. Miller and M. I. Lerner, *Nanomaterials*, 2022, **12**, 2523.
99 J. C. Toniolo, A. S. Takimi and C. P. Bergmann, *Mater. Res. Bull.*, 2010, **45**, 672–676.
100 C. Italiano, J. Llorca, L. Pino, M. Ferraro, V. Antonucci and A. Vita, *Appl. Catal., B*, 2020, **264**, 118494.
101 F. Huang, C. Chen, F. Wang, B. Wang, L. Zhang, S. Lu and K. Li, *Catal. Surv. Asia*, 2017, **21**, 143–149.
102 J. Y. Luo, M. Meng, X. Li, X. G. Li, Y. Q. Zha, T. D. Hu, Y. N. Xie and J. Zhang, *J. Catal.*, 2008, **254**, 310–324.
103 F. L. S. Carvalho, Y. J. O. Asencios, J. D. A. Bellido and E. M. Assaf, *Fuel Process. Technol.*, 2016, **142**, 182–191.
104 T. A. Maia, J. M. Assaf and E. M. Assaf, *Fuel Process. Technol.*, 2014, **128**, 134–145.
105 A. Filtschew, K. Hofmann and C. Hess, *J. Phys. Chem. C*, 2016, **120**, 6694–6703.
106 E. Sartoretti, C. Novara, F. Giorgis, M. Piumetti, S. Bensaid, N. Russo and D. Fino, *Sci. Rep.*, 2019, **9**, 3875.
107 X. Li, X. Liu, J. Hao, L. Li, Y. Gao, Y. Gu, Z. Cao and J. Liu, *ACS Omega*, 2022, **7**, 24646–24655.
108 N. Mironova-Ulmane, A. Kuzmin, I. Sildos and M. Pärs, *Open Phys.*, 2011, **9**, 1096–1099.
109 G. Jones, J. G. Jakobsen, S. S. Shim, J. Kleis, M. P. Andersson, J. Rossmeisl, F. Abild-Pedersen, T. Bligaard, S. Helveg, B. Hinnemann, J. R. Rostrup-Nielsen, I. Chorkendorff, J. Sehested and J. K. Nørskov, *J. Catal.*, 2008, **259**, 147–160.
110 M. L. Dieuzeide and N. Amadeo, *Chem. Eng. Technol.*, 2010, **33**, 89–96.

111 C. K. Cheng, S. Y. Foo and A. A. Adesina, *Catal. Commun.*, 2010, **12**, 292–298.
112 T. Pairojpiriyakul, E. Croiset, W. Kiatkittipong, K. Kiatkittipong, A. Arpornwichanop and S. Assabumrungrat, *Int. J. Hydrogen Energy*, 2013, **38**, 4368–4379.
113 J. Dobosz, M. Cichy, M. Zawadzki and T. Borowiecki, *J. Energy Chem.*, 2018, **27**, 404–412.
114 A. Carrero, A. J. Vizcaíno, J. A. Calles and L. García-Moreno, *J. Energy Chem.*, 2017, **26**, 42–48.
115 M. Surendar, T. V. Sagar, B. H. Babu, N. Lingaiah, K. S. R. Rao and P. S. S. Prasad, *RSC Adv.*, 2015, **5**, 45184–45193.
116 S. A. Ghungrud and P. D. Vaidya, *Int. J. Hydrogen Energy*, 2020, **45**, 9440–9450.
117 H. Zhou, S. Liu, F. Jing, S.-Z. Luo, J. Shen, Y. Pang and W. Chu, *Ind. Eng. Chem. Res.*, 2020, **59**, 17259–17268.
118 C. A. Schwengber, H. J. Alves, R. A. Schaffner, F. A. Da Silva, R. Sequinel, V. R. Bach and R. J. Ferracin, *Renewable Sustainable Energy Rev.*, 2016, **58**, 259–266.
119 C. K. S. Choong, Z. Zhong, L. Huang, Z. Wang, T. P. Ang, A. Borgna, J. Lin, L. Hong and L. Chen, *Appl. Catal., A*, 2011, **407**, 145–154.
120 N. Charisiou, S. Douvartzides, G. Siakavelas, L. Tzounis, V. Sebastian, V. Stolojan, S. Hinder, M. Baker, K. Polychronopoulou and M. Goula, *Catalysts*, 2019, **9**, 676.
121 A. J. Reynoso, J. L. Ayastuy, U. Iriarte-Velasco and M. A. Gutiérrez-Ortiz, *J. Environ. Chem. Eng.*, 2022, **10**, 107402.
122 R. L. Manfro, T. P. M. D. Pires, N. F. P. Ribeiro and M. M. V. M. Souza, *Catal. Sci. Technol.*, 2013, **3**, 1278–1287.
123 S. H. Cho and D. J. Moon, *J. Nanosci. Nanotechnol.*, 2011, **11**, 7311–7314.
124 A. Morales-Marín, U. Iriarte-Velasco, M. Á. Gutiérrez-Ortiz and J. L. Ayastuy, *Catalysts*, 2022, **12**, 668.